Transcription and splicing dynamics during early *Drosophila* development

Pedro Prudêncio [1, 2 §], Kenny Rebelo [1§$], Rosina Savisaar [1§], Rui Gonçalo Martinho[1, 2, 3*] and Maria Carmo-Fonseca[1*]

[1] Instituto de Medicina Molecular João Lobo Antunes, Faculdade de Medicina, Universidade de Lisboa, Portugal.

[2] Center for Biomedical Research, Universidade do Algarve, Faro, Portugal.

[3] iBiMED, Departamento de Ciências Médicas, Universidade de Aveiro, Portugal

[§]These authors have contributed equally to the work.

[$]Present address: Donnelly Centre, University of Toronto, Toronto, ON M5S 3E1, Canada

[*]Joint corresponding authors: carmo.fonseca@medicina.ulisboa.pt and rgmartinho@ua.pt

RUNNING TITLE: Transcription and splicing dynamics in *Drosophila*

KEYWORDS: splicing kinetics; Pol II pausing; transcription termination; NET-seq; *Drosophila melanogaster* embryo

ABSTRACT

Widespread co-transcriptional splicing has been demonstrated from yeast to human. However, measuring the kinetics of splicing relative to transcription has been hampered by technical challenges. Here, we took advantage of native elongating transcript sequencing (NET-seq) to identify the position of RNA polymerase II (Pol II) when exons become ligated in the newly synthesized RNA. We analyzed *Drosophila melanogaster* embryos because the genes transcribed initially during development have few and short introns (like yeast genes), whereas genes transcribed later contain multiple long introns (more similar to human genes). We detected spliced NET-seq reads connected to Pol II molecules that were positioned just a few nucleotides downstream of the 3' splice site. Although the majority of splice junctions were covered by spliced reads, many introns remained unspliced, resulting in a complex range of heterogeneity in splicing dynamics. Introns that show splicing completion before Pol II has reached the end of the downstream exon are necessarily intron-defined. As expected, we found a relationship between the proportion of spliced reads and intron size. However, intron definition was observed at all intron sizes. Both canonical and recursive splicing were associated with a higher Pol II density, suggesting a splicing-coupled mechanism that slows down transcription elongation. We further observed that transcription termination was very efficient for isolated genes but that the presence of an overlapping antisense gene was often associated with transcriptional read-through. Taken together, our data unravels novel dynamic features of Pol II transcription and splicing in the developing *Drosophila* embryo.

INTRODUCTION

It is by now largely accepted that splicing can happen, and often does happen, whilst transcription is still in progress (Ameur et al. 2011; Khodor et al. 2011; Beyer and Osheim 1988; Brugiolo et al. 2013; Carrillo Oesterreich et al. 2010; Windhager et al. 2012; Nojima et al. 2015; Alpert et al. 2017). It is also known that the processes of splicing and transcription are tightly interlinked. The RNA Polymerase II (Pol II) elongation rate can affect exon inclusion (Fong et al. 2014; Maslon et al. 2019; Aslanzadeh et al. 2018), and many of the proteins involved in splicing associate with the Pol II C-terminal domain (CTD) (Hsin and Manley 2012; Emili et al. 2002; David et al. 2011; Görnemann et al. 2011; Morris and Greenleaf 2000; Nojima et al. 2018). Conversely, splicing may also affect transcription, with evidence suggesting that Pol II slows down at exons (Alexander et al. 2010; Carrillo Oesterreich et al. 2010; Jonkers et al. 2014; Mayer et al. 2015; Veloso et al. 2014), potentially to allow for splicing to complete.

The exact timing and duration of splicing remain more controversial. A nascent RNA sequencing study (Carrillo Oesterreich et al. 2016) showed that in *Saccharomyces cerevisiae*, splicing could occur as soon as the 3' splice site had emerged from the transcription machinery, suggesting that splicing may be completed immediately after intron transcription. Previous attempts to determine the duration of splicing *in vivo* had returned estimates ranging from a few seconds to several hours (Alpert et al. 2017). The lowest of these estimates, such as the few-second estimate reported in Martin et al. (2013), are consistent with splicing being completed right after the 3' splice site is transcribed. However, the much longer estimates obtained in most previous studies (Alpert et al. 2017) would imply that by the time an intron is excised, Pol II would have transcribed hundreds, if not thousands, of nucleotides beyond the respective 3' splice site. Importantly, the technique used by Carrillo Oesterreich et al. (2016) does not measure time but rather Pol II progression (i.e. how far Pol II has elongated from the 3' splice site by the time the intron has been spliced). If Pol II was stalling at the start of exons, then splicing could still take a relatively long time, as suggested by most previous work (Alpert et al. 2017), with little concomitant Pol II progression, as observed in Carrillo Oesterreich et al. (2016). However, the authors found no evidence that Pol II was pausing after the 3' splice site, suggesting that in many

cases, splicing was indeed occurring in no more than a couple of seconds (Carrillo Oesterreich et al. 2016).

More recently, two long-read nascent RNA sequencing studies addressed the timing of splicing in metazoa. One reported little immediate splicing in human and *Drosophila* cells, with most splicing occurring when Pol II had elongated thousands of nucleotides past the intron (Drexler et al. 2020). Another found that splicing occurred at a median distance of 141 nt from the 3' splice site in mouse cells (Reimer et al. 2020).

Here, we have used Native Elongating Transcript Sequencing (NET-seq) (Churchman and Weissman 2011; Nojima et al. 2015) to study the dynamic properties of transcription and co-transcriptional splicing during early stages of development in *Drosophila melanogaster* embryos. An advantage of this model system is that compared to human, the *Drosophila* genome is more compact (Graveley et al. 2011) and thus the coverage of NET-seq reads on intragenic regions is higher. Henceforth, we will refer to NET-seq adapted for use in *Drosophila* as *d*NET-seq.

Drosophila early development is characterized by rapid mitotic cycles that lack cytokinesis, resulting in nuclear proliferation in a syncytial cytoplasm (Campos-Ortega 1985; Laver et al. 2015). During these initial mitotic divisions, which impose significant constraints on transcription and splicing (Shermoen and O'Farrell 1991; Rothe et al. 1992; Guilgur et al. 2014; Martinho et al. 2015; Sandler et al. 2018; Kwasnieski et al. 2019), the embryo largely relies on maternally deposited mRNAs. Subsequently, the duration of the cell cycle is progressively expanded, membranes form between the nuclei and segregate them into cells, and the zygotic transcriptome starts to be fully expressed (Campos-Ortega 1985; Yuan et al. 2016; Blythe and Wieschaus 2015a). The stage at which the embryo switches from relying on maternally deposited mRNAs and proteins to undergoing its own transcription is known as the mid-blastula transition (MBT). A few genes become transcriptionally active before MBT (pre-MBT genes) (Kwasnieski et al. 2019). Pre-MBT genes are characterized by containing few, short introns (like yeast genes), whereas genes expressed later have multiple long introns (more similar to human genes). By performing *d*NET-seq in the developing *Drosophila* embryo, we have unravelled novel dynamic features of Pol II transcription and splicing.

RESULTS

Native elongating transcript sequencing in *Drosophila* embryos (*d*NET-seq)

Our first task was to adapt the NET-seq method for use in *Drosophila* embryos. In *Drosophila* embryos, nuclei are initially located in the interior of the egg, but after 8 mitotic cycles about three quarters of the nuclei start to migrate outwards. By cycle 10, the migrating nuclei become evenly distributed in a monolayer under the egg surface (Campos-Ortega 1985; Laver et al. 2015). The next mitotic divisions (cycles 10-13) take place almost synchronously in this monolayer of blastoderm nuclei, still syncytial. During interphase of cycle 14, membranes form between all of the peripheral nuclei, segregating them into separate cells. As soon as they are formed, the new cells start the morphogenetic movements that characterize gastrulation and result in a multi-layered embryo. During the 14th interphase, the global mitotic synchrony ceases, as cells start to become committed to specific developmental fates. During gastrulation, the embryo trunk (also known as the germ-band) elongates in the antero-posterior axis and narrows in the dorso-ventral axis; this process is termed germ-band extension (Campos-Ortega 1985; Laver et al. 2015).

We collected embryos at 2-3 hours after fertilization (referred to as early embryos) and 4-6 hours after fertilization (referred to as late embryos) (**Figure 1A**). Analysis of embryos stained with a fluorescent dye to visualize DNA (**Figure 1B**) revealed that early embryos were predominantly in cycle 14 (stage 5), whereas the majority of late embryos were in the late stage of germ-band extension (stage 10; **1C**).

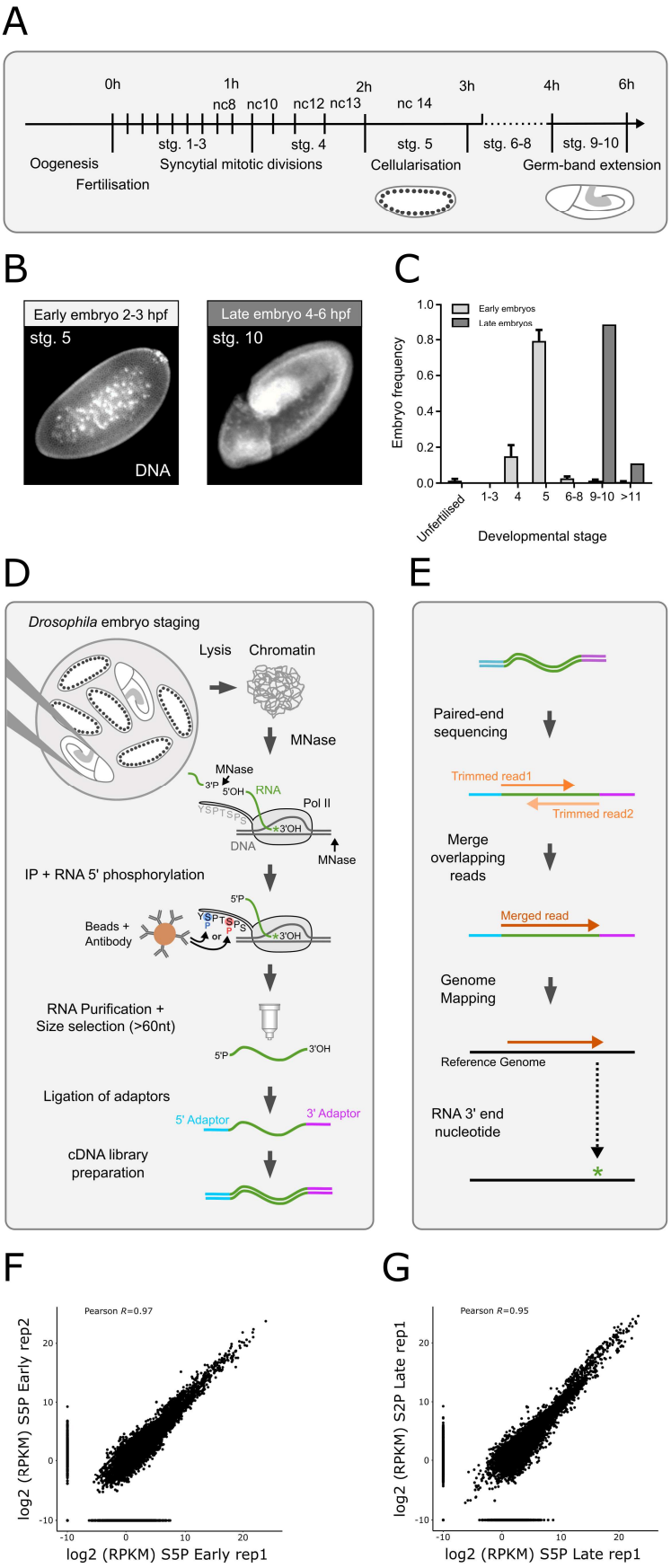
A
0h
1h
2h
3h
4h
6h
nc8
nc10
nc12
nc13
nc 14
stg. 1-3
stg. 4
stg. 5
stg. 6-8
stg. 9-10
Oogenesis
Fertilisation
Syncytial mitotic divisions
Cellularisation
Germ-band extension
B
Early embryo 2-3 hpf
stg. 5
DNA
Late embryo 4-6 hpf
stg. 10
C
Early embryos
Late embryos
Embryo frequency
Unfertilised
1-3
4
5
6-8
9-10
>11
Developmental stage
D
Drosophila embryo staging
Lysis
Chromatin
MNase
RNA
Pol II
DNA
IP + RNA 5' phosphorylation
Beads +
Antibody
RNA Purification +
Size selection (>60nt)
Ligation of adaptors
5' Adaptor
3' Adaptor
cDNA library
preparation
E
Paired-end
sequencing
Trimmed read1
Trimmed read2
Merge
overlapping
reads
Merged read
Genome
Mapping
Reference Genome
RNA 3' end
nucleotide
F
Pearson R=0.97
log2 (RPKM) S5P Early rep2
log2 (RPKM) S5P Early rep1
G
Pearson R=0.95
log2 (RPKM) S2P Late rep1
log2 (RPKM) S5P Late rep1

Figure 1. Native elongating transcript sequencing in *Drosophila* embryos.
(A) Timeline of *Drosophila* early embryonic development. **(B)** Representative images (stained for DNA) of embryos in nuclear cycle 14 (stage 5) and late germ-band expansion (stage 10). **(C)** The graph depicts the developmental stage of embryos sorted into the "early" and "late" groups. **(D)** Outline of the *d*NET-seq experimental protocol. **(E)** Outline of *d*NET-seq data analysis. **(F)** Density of uniquely aligned reads per gene (RPKM in log2 scale) for two *d*NET-seq/S5P biological replicates from early embryos (Pearson's correlation, R = 0.97). **(G)** Density of uniquely aligned reads per gene (RPKM in log2 scale) from late embryos analysed by *d*NET-seq/S5P and *d*NET-seq/S2P (Pearson's correlation, R = 0.95).

NET-seq relies on the intrinsic stability of ternary transcription complexes formed by RNA polymerase II (Pol II), the DNA template and nascent RNA to isolate Pol II elongation complexes by immunoprecipitation without crosslinking. NET-seq was initially established in yeast to visualize the genomic position of the active site of Pol II by identifying the 3' ends of the nascent RNA (Churchman and Weissman 2011). The method was later applied to mammalian cells and termed mNET-seq (Nojima et al. 2015, 2016). Because solubilisation of Pol II complexes under native conditions is typically incomplete in metazoan cells (Kimura et al. 1999), the mNET-seq protocol uses micrococcal nuclease (MNase) digestion of isolated chromatin. In adapting mNET-seq to *Drosophila* embryos, we optimized buffers and washing conditions to purify the chromatin fraction from manually sorted embryos, solubilize the transcription complexes with MNase digestion and immunoprecipitate Pol II with antibodies. We used rabbit polyclonal antibodies raised against synthetic peptides of the YSPTSPS repeat of the CTD of the largest Pol II subunit in *Saccharomyces cerevisiae*, phosphorylated at either S5 (ab5131 Abcam) or S2 (ab5095 Abcam). Both antibodies have been extensively used for chromatin immunoprecipitation experiments and shown to react with *Drosophila melanogaster* (Dahlberg et al. 2015).

To enable directional sequencing, the 5' hydroxyl (OH) generated by MNase digestion of RNA was first converted to a 5' phosphate by T4 polynucleotide kinase (**Figure 1D**). RNA was then purified from the immunoprecipitated Pol II complexes and size-selected using an RNA purification kit procedure that combines a unique buffer system with a column technology (see the methods section for more detail). RNAs with a size above 60 nucleotides (nt) were used for subsequent ligation of specific adapters to the 5' P and 3' OH ends of each RNA fragment followed by PCR-based preparation of a cDNA library for high-throughput Illumina sequencing (**Figure 1D**). After sequencing, adapter

sequences were trimmed and paired-end reads with sequence overlaps were merged into a single read that spans the full length of the original RNA fragment (dark orange; **Figure 1E**). The resulting single reads were aligned to the *Drosophila* reference genome. The nucleotide at the 3' end of each RNA fragment was identified and its genomic position recorded (asterisk; **Figure 1E**).

Two to three NET-seq libraries were independently prepared from early and late embryos using S5P antibody; three additional libraries were prepared from late embryos using S2P antibody. Each library was sequenced to a high coverage with a read length of 150 bp (**Figure S1A**). Experimental reproducibility was demonstrated by strong agreement of uniquely aligned read density between biological replicates (**Figure 1F and S1 B, C**). Very similar values of read density were also observed in late embryo samples prepared with S5P and S2P antibodies (**Figure 1G**), suggesting that in *Drosophila* embryos, the CTD of elongating Pol II is phosphorylated on both serine 5 and serine 2 positions.

_d_NET-seq reveals co-transcriptional splicing associated with Pol II phosphorylated on CTD serine 5.

NET-seq captures not only the final (3' OH end) nucleotide of nascent RNA but also the 3' OH end of RNAs that associate with the Pol II elongation complex (Nojima et al. 2015, 2018; Schlackow et al. 2017). Notably, in humans, mNET-seq of Pol II phosphorylated on CTD serine 5 detected splicing intermediates formed by cleavage at the 5' splice site after the first splicing reaction. The presence of such intermediates manifests as an enrichment of reads whose 3' ends map precisely to the last nucleotide of an exon. In both early and late *Drosophila* embryos, we indeed observed large peaks of *d*NET-seq/S5P reads mapping to the last nucleotide of spliced exons, as shown for the *kuk* gene (asterisk; **Figure 2A**. We also detected *d*NET-seq/S5P peaks at the last nucleotide of introns, as shown for the *eEF1alpha1* gene (asterisk; **Figure 2B**); enrichment for these reads results from co-immunoprecipitation of released intron lariats after completion of the splicing reaction (**Figure 2B**). In addition, we observed reads corresponding to mature snRNAs engaged in co-transcriptional spliceosome assembly, suggesting that *d*NET-seq was capturing the free 3' OH ends of the snRNAs.

(**Figure 2C**). We found prominent peaks at the end of spliceosomal U1, U2, U4 and U5 snRNAs. As expected, no peak was detected mapping to the end of the U3 snRNA, which is involved in the processing of pre-rRNA synthesized by Pol I. Noteworthy, we observed an accumulation of *d*NET-seq signal at the end of U6 snRNA (**Figure S2A**), contrasting with a lack of peak observed in mammalian cells (Nojima et al. 2018). This is consistent with the finding that mammalian U6 snRNAs contain a 2',3'-cyclic phosphate terminal group at the 3' end, whereas U6 3' ends in *Drosophila* embryos consist of either P or OH (Lund and Dahlberg 1992).

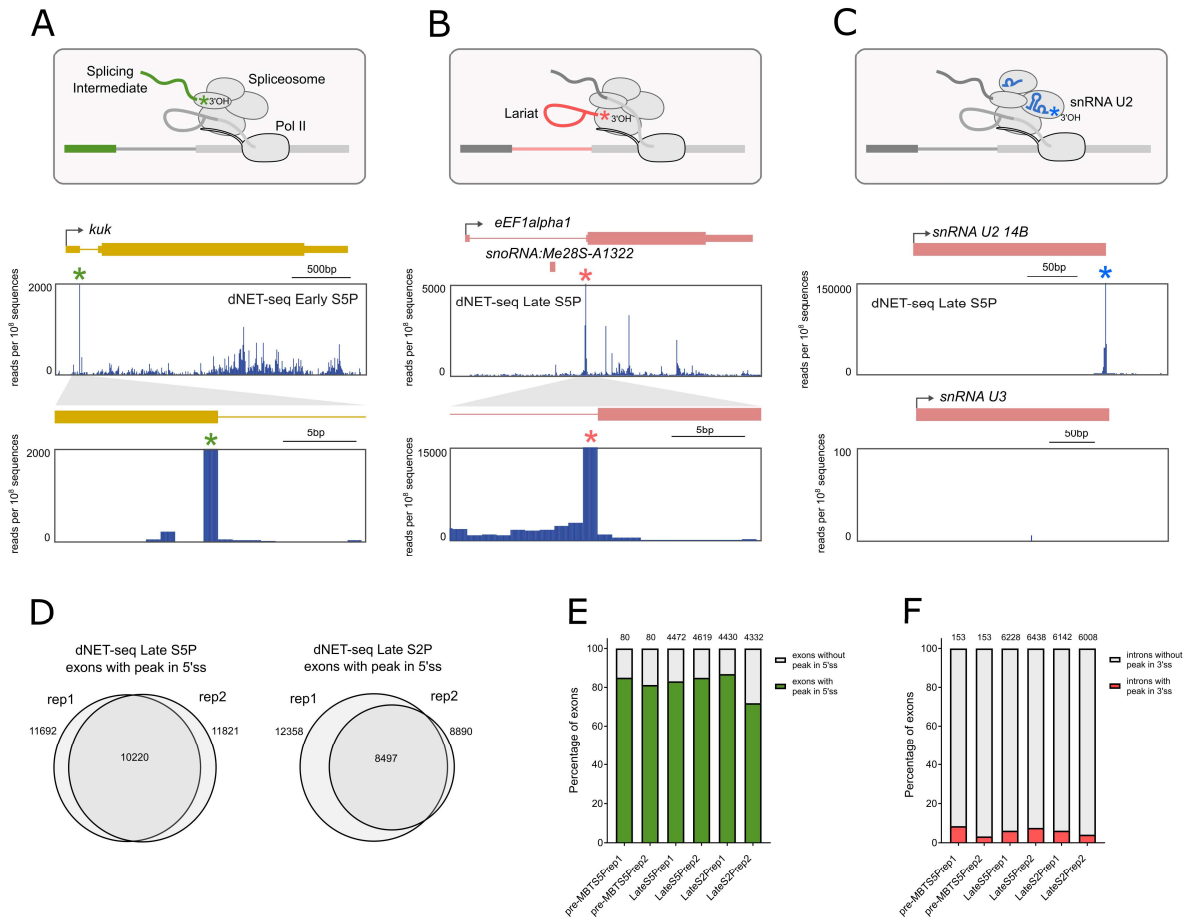

Figure 2. Co-transcriptional splicing associated with Pol II phosphorylated on CTD serine 5. (A-C) *d*NET-seq/S5P profiles over the indicated genes in late embryos. The diagrams outline the 3' OH ends generated by co-transcriptional cleavage at the 5' splice site (green, **A**), the 3' splice site (red, **B**) and the free 3' OH end of spliceosomal snRNAs (blue, **C**). Arrows indicate the direction of transcription. Exons are represented by boxes. Thinner boxes represent UTRs. Introns are represented by lines connecting the exons. Asterisks denote the peak at the end of the exon (**A**), the end of the intron (**B**), and the end of the U2 snRNA gene (**C**). (**D**) Comparison (Venn diagrams) of exons with a splicing intermediate peak detected in biological replicates of *d*NET-seq/S5P and *d*NET-seq/S2P libraries. (**E, F**) Frequency of peaks corresponding to splicing intermediates (**E**) and released intron lariats (**F**) in pre-MBT genes and genes expressed in late embryos. Only genes with the highest read density (fourth quartile) were considered.

To quantify how many constitutively spliced exons have *d*NET-seq peaks at the end, we applied an algorithm that finds nucleotides where the NET-seq read density is at least three standard deviations above the transcript mean in a local region defined by 100 bp upstream and downstream (Churchman and Weissman 2011; Prudêncio et al. 2020). Upon analysing replicates of *d*NET-seq/S5P and *d*NET-seq/S2P libraries, we identified over 10,000 exons showing splicing intermediate peaks (**Figure 2D**). As peaks were more frequently detected on exons of genes with higher read density (**Figure S2B**), we classified the exons into four groups (quartiles) based on the *d*NET-seq read density of the corresponding gene and restricted the analysis to exons in the fourth quartile, i.e., from genes with the highest read density. The results show that splicing intermediate peaks are detected in approximately 80% of all constitutively spliced exons. The proportion is similar for pre-MBT genes, i.e, zygotic genes that start to be transcribed before cycle 14 and remain active thereafter (Chen *et al.*, 2013), and for genes expressed in late embryos (**Figure 2E**). Similar proportions were found in the S5P and the S2P datasets (**Figure 2E**). We then used the same methodology and the same set of genes to detect peaks at the last intronic nucleotide, corresponding to released intron lariats. Such peaks were detected in less than 10% of introns (**Figure 2F**).

Taken together, these results demonstrate that in *Drosophila* embryos, co-transcriptional splicing is associated with Pol II phosphorylated at the CTD serine 5 position, as previously reported in mammalian cells (Nojima et al. 2015; Schlackow et al. 2017; Nojima et al. 2018).

_d_NET-seq specifically captures nascent RNA.

To validate that we were detecting nascent transcription in *Drosophila* embryos, we analysed maternal mRNAs that are transcribed during oogenesis and loaded into the egg (**Figure 3A**). As expected, maternal transcripts such as *bicoid* (**Figure 3B**), *nanos* (**Figure S3A**), *gurken* (**Figure S3B**) and *Rab32* (**Figure S3C**) were detected by RNA-seq in embryos collected 2-3 hours after fertilization, but *d*NET-seq signal over these genes was negligible. However, robust *d*NET-seq signal was found at the *pumilio* gene (**Figure S3D**). Expression of this gene was considered to be exclusively maternal based on RNA-seq (Lott et al. 2011) and Pol II ChIP-seq data (Chen et al. 2013), but a GRO-seq study

detected *pumilio* nascent transcripts in embryos collected 2-2.5 hours post-fertilisation (Saunders et al. 2013). The detection of *pumilio* RNA in early embryos by GRO-seq and *d*NET-seq highlights the sensitivity of these two techniques in capturing low-level nascent transcripts.

Strong *d*NET-seq signal was detected in early embryos over the bodies of pre-MBT genes such as *snail* (**Figure 3C**), *fushi tarazu* (**Figure S3E**) and *odd skipped* (**Figure S3F**). Altogether, we examined 117 previously identified pre-MBT genes. A characteristic feature of these genes is that they are short in length with few if any introns (De Renzis et al. 2007; Ali-Murthy et al. 2013; Kwasnieski et al. 2019; Heyn et al. 2014). In contrast, most genes expressed in late embryos contain multiple introns, as shown for *Akap200* (**Figure 3D**), *His3.3A* (**Figure S3G**) and *twinstar* (*tsr*) (**Figure S3H**). Analysis of *d*NET-seq datasets from late embryos revealed widespread signal on introns and regions downstream of the polyadenylation site, further confirming that the technique is capturing nascent transcripts.

To conclude, robust *d*NET-seq signal was recovered from zygotically but not from maternally expressed transcripts. In addition, we detected reads mapping to introns and downstream of the poly-adenylation site. These findings suggest that *d*NET-seq is indeed specifically targeting the nascent transcriptome.

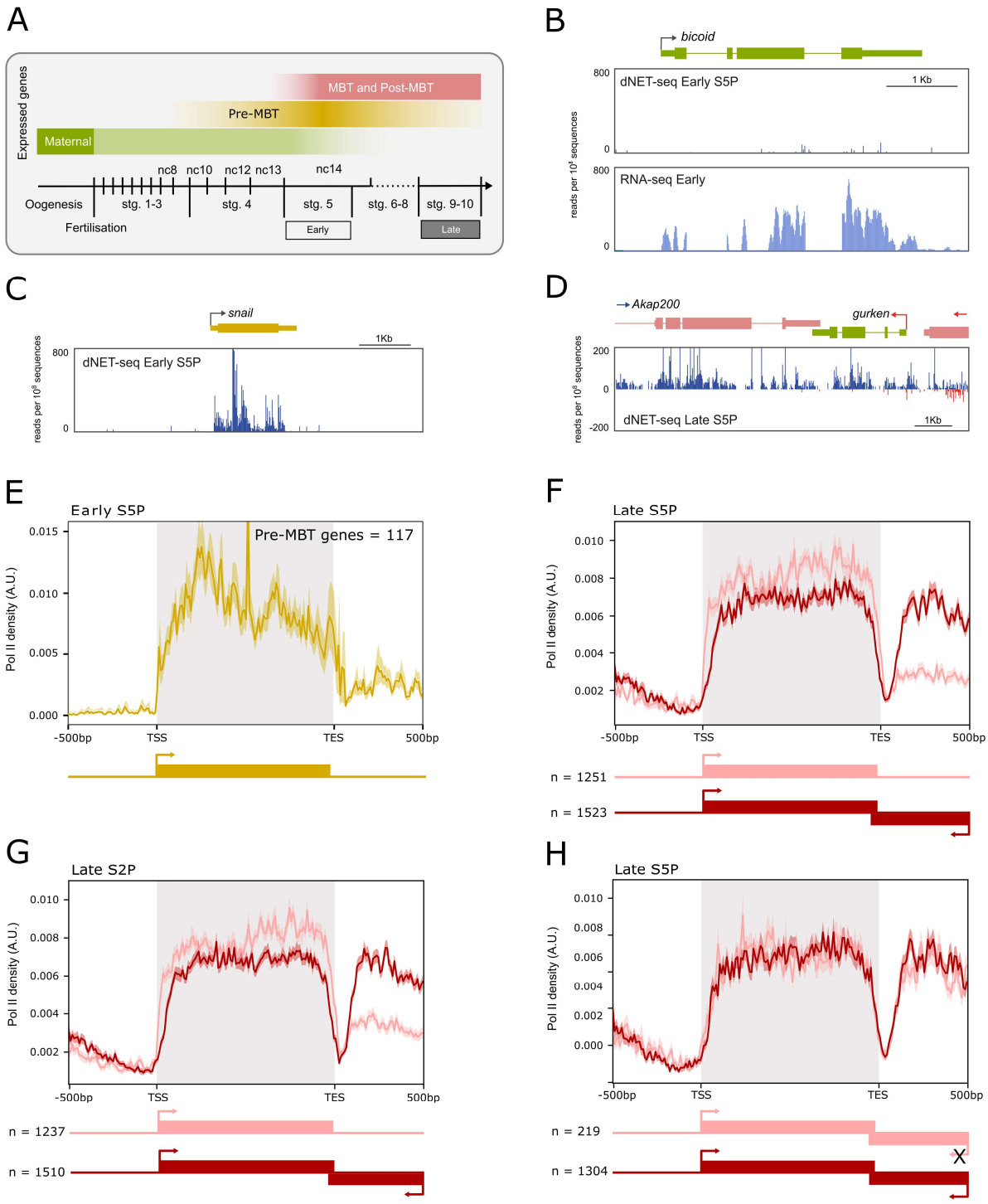

Figure 3. Transcription over gene bodies and beyond the TES. (A) The diagram illustrates the temporal expression of maternal, pre-MBT, MBT, and post-MBT genes during *Drosophila* embryonic development. For all datasets in **(B-H)**, only replicate 1 is shown. **(B-D)** *d*NET-seq/S5P and RNA-seq profiles over the maternal gene *bicoid* (**B**), the pre-MBT gene *snail* (**C**), and the post-MBT gene *Akap200* (**D**). Reads that aligned to the positive strand are in blue, and reads that aligned to the negative strand are in red. **(E-H)** Normalized metagene analysis in arbitrary units (A.U.). The *d*NET-seq signal is depicted along the normalized gene length (grey background), as well as 500 bp upstream of the transcription start site (TSS) and 500 bp downstream of the transcription end site (TES). **(E)** *d*NET-seq/S5P signal on pre-MBT genes in early embryos. **(F)** *d*NET-seq/S5P signal on transcriptionally active genes in late embryos; the signal over genes that have the 3' UTR overlapped by an antisense

gene is depicted in dark red, while the signal over genes with no other genes within 500 bp is depicted in light red. **(G)** *d*NET-seq/S2P signal on transcriptionally active genes in late embryos. **(H)** *d*NET-seq/S5P signal on transcriptionally active genes in late embryos; the signal over genes that have the 3' UTR overlapped by a transcriptionally active antisense gene is depicted in dark red, while the signal over genes with the 3' UTR overlapped by a transcriptionally inactive antisense gene is depicted in light red.

_d_NET-seq reveals transcriptional read-through associated with the presence of overlapping antisense genes.

Having confirmed that *d*NET-seq was capturing nascent RNA, we next investigated the distribution of Pol II density over transcript regions in early and late embryos. The *d*NET-seq profiles over individual genes (**Figure 3C, D and S3**) do not show the characteristic higher read density near the promoter, as previously described in mammalian cells (Nojima et al. 2015; Mayer et al. 2015). This is most likely because Pol II typically pauses ~30-60 bp downstream of the transcription start site (TSS) (Kwak et al. 2013) and in our *d*NET-seq approach we enrich for RNAs longer than 60 nt (**Figure S1D**); thus, we only record the position of polymerases that have transcribed at least 60 bp past the TSS.

We then turned our attention to the *d*NET-seq signal around polyadenylation sites (also known as the transcription end sites or TES). Many genes, such as *Akap200* (**Figure 3D**), *His3.3A* (**Figure S3G**) and *tsr* (**Figure S3H**), have significant *d*NET-seq/S5P signal after the TES, indicative that in these cases, Pol II continues to transcribe after cleavage and polyadenylation. We noted that the 3' UTR of these three genes is overlapped by another gene (*gurken, Nepl3,* and *IntS1,* respectively), which is transcribed in the opposite direction. We therefore asked whether transcriptional read through is related to the presence of an overlapping convergent gene. In order to identify all genes that are transcriptionally active in late embryos, we used a strategy adapted from GRO-seq analysis (Core et al. 2008) that relies on read density in gene desert regions as background reference for absence of transcription. Very large intergenic regions (gene deserts) were divided into 50kb windows, and read densities were calculated by dividing read counts in each window by the window length in bp (**Figure S4A**). Genes with *d*NET-seq signal over the gene body (in RPKM) above the 90th percentile of read density for all intergenic regions analysed were considered to be transcriptionally active (**Figure S4B**).

We identified approximately 7 thousand active genes, and similar results were obtained from *d*NET-seq/S5P and *d*NET-seq/S2P datasets (**Figure S4C**). This set of active genes includes over 85% of the 3500 genes previously identified as actively transcribed after the mid-blastula transition (MBT) based on ChIP-seq experiments (Chen et al. 2013). Next, we divided the genes transcribed in late embryos into two groups, depending on whether their 3' UTR was or was not overlapped by another convergent gene. The metagene analysis shows that on all transcribed genes, the *d*NET-seq/S5P signal is abruptly reduced at the TES (**Figure 3F**). This is expected, as when Pol II reaches this site, the nascent transcript is cleaved and polyadenylated and therefore there is no RNA to be sequenced. However, the presence of nascent transcripts after the TES, indicating that Pol II fails to terminate transcription after cleavage and polyadenylation, is mainly observed on genes that have the 3' UTR overlapped by an antisense gene (**Figure 3F**). Similar results were observed after metagene analysis of *d*NET-seq/S2P datasets (**Figure 3G**), confirming an association between transcriptional read-through and genomic architecture at the TES. We then asked whether transcriptional read-through depends on the transcriptional activity of the overlapping antisense (convergent) gene. Using the methodology described above to identify transcribed genes, we found that the vast majority (>80%) of overlapping convergent genes were transcriptionally active and only 219 genes were silent. The metagene analysis shown in **Figure 3H** clearly indicates that transcription of the convergent overlapping gene is not required for inefficient termination at the overlapped TES.

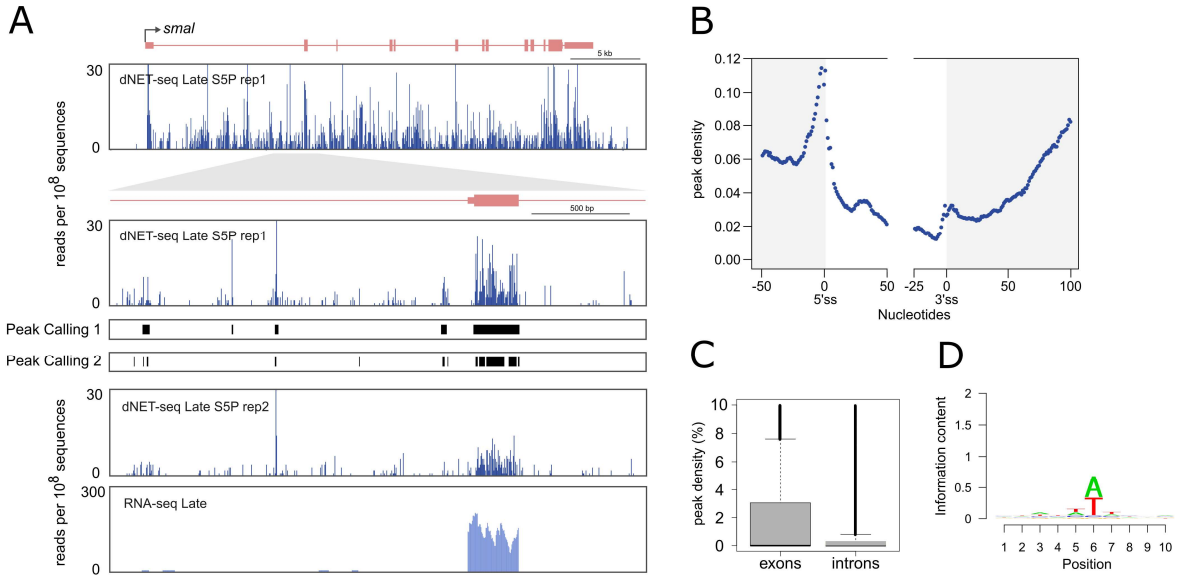

Figure 4. Evidence for Pol II pausing after the 3' splice site.
(**A**) *d*NET-seq/S5P and RNA-seq profiles over the post-MBT gene *smoke alarm* (*smal*). The number of NET-seq reads is depicted at two magnification levels in two biological replicates. For replicate 1, the line "Peak Caller 1" shows peaks called using the "large peaks" setting, which is appropriate for detecting larger regions of putative Pol II pausing. The line "Peak Caller 2" shows peaks called using the "small peaks" setting, which provides higher spatial resolution and has been used for subsequent analyses. RNA-seq data for the same regions is also shown. (**B**) Metagene analysis of Pol II peak density estimated from *d*NET-seq/S5P datasets from late embryos (replicate 1). Peak density has been calculated as the proportion of introns that overlap with a peak at any given position. The last 50 nucleotides of exons, the first 50 nucleotides of introns, the last 25 nucleotides of introns, and the first 100 nucleotides of exons are shown. Only internal and fully coding exons from transcriptionally active genes that are at least 100 nucleotides long are shown. Exons shorter than 150 nucleotides contribute to both the exon end and start. Only introns that were at least 50 nt long were considered. **(C)** Peak density in the exons and introns of transcriptionally active genes (*d*NET-seq/S5P, replicate 1). Peak density has been defined as the percentage of nucleotides within a given exon or intron that overlap with a significant peak. **(D)** Sequence logo of nucleotide frequencies within a 10-nt window around the 5' ends of NET-seq reads. The combined height of the bases at each position is proportional to the information content. Position 6 corresponds to the 5'-most nucleotide of the read. Putative internal priming reads, as well as reads mapping to the last nucleotide of exons or introns (possible splice intermediate and intron lariat reads) were ignored.

The vast majority of pre-MBT genes do not show transcriptional read-through (**Figure 3C and S3E, F**). This may relate to the fact that for the majority of these genes (65), there is no other gene on either strand within a region of 500 bp downstream of the TES (referred to henceforth as 'isolated genes'), as shown for *tailless (tll)* (**Figure S4D**). Another 26 pre-MBT genes are embedded in larger genes, as shown for *nullo*, which is located within a long intron of the *CG12541* gene (**Figure S4E**). A smaller group of pre-MBT genes (21) have neighbouring genes located on either strand within a region of 500 bp downstream of the TES, as shown for *Elba2* (**Figure S4F**). We further identified 5 pre-MBT

genes that have the 3' UTR overlapped by an antisense convergent gene, as shown for *spook (spo)* (**Figure S4G**). Transcriptional read-through was observed in these pre-MBT genes (**Figure S4G**). Importantly, the proportion of isolated genes is significantly higher among pre-MBT genes (65/117 or ~56%) than among late genes (1251/7233 or ~17% of all transcriptionally active genes for replicate 1 S5P) ($P < 2.2 * 10^{-16}$, one-tailed binomial test). This may suggest that pre-MBT genes are under selection to avoid overlaps with other genes, promoting efficient transcriptional termination.

In conclusion, *d*NET-seq reveals a strong correlation between inefficient transcription termination at the cleavage and polyadenylation site, and presence of an antisense convergent gene overlapping the TES. The vast majority of genes that start to be transcribed before the mid-blastula transition, when the mitotic cycles are still very short, do not have the TES overlapped by other genes and are efficiently terminated. In contrast, many genes that start to be transcribed after the mid-blastula transition, when the mitotic cycles become much longer, show transcriptional read through and are overlapped by an antisense convergent gene.

Evidence for Pol II pausing after the 3' splice site

We next asked whether there was evidence of Pol II pausing around splice sites, which could suggest interactions between the splicing and transcription machineries. The number of nascent RNA reads whose 3' ends map at a particular genomic position is proportional to the number of Pol II molecules at that position. Thus, Pol II pause sites can be detected as local peaks in read density (Churchman and Weissman 2011; Larson et al. 2014). For this analysis, we excluded signal from co-transcriptional splicing (i.e., reads that map to the very last nucleotide of introns and exons were discarded). In addition, we specifically focused on the S5P data, as co-transcriptional splicing has been linked to S5P in humans (Nojima et al. 2015). Many strong peaks of *d*NET-seq/S5P signal were observed over both exons and introns (**Figure 4A**).

Our next task was to identify such pause sites more systematically. A difficulty of this analysis is that transcripts with higher initiation rates will contain more reads and thus peaks are more likely to be detected than in more lowly transcribed genes. To control for this confound, we developed a peak

calling algorithm that detects regions where the local read density is significantly higher than expected by chance, given the over-all read density of the transcript (**Figure 4A;** see also the methods section). We emphasize that for detecting splice intermediate peaks (**Figure 2D-F)**, we used a peak calling method that looks for significant single-nucleotide positions (Churchman and Weissman 2011), whereas this new method detects putative pause regions of variable length.

We then aligned exons and introns on the splice sites and calculated the average peak density at each position. Exons have a higher over-all peak density than introns (mean proportion of nucleotides in peaks ~0.022/~0.015 for replicate 1/replicate 2 introns and ~0.043/~0.034 for replicate 1/replicate 2 exons; $P < 2.2 * 10^{-16}$ for both replicates; two-tailed Mann-Whitney *U*-test with the peak densities of individual introns/exons as data points), suggesting that the elongation rate is decreased over exons (**Figure 4C**). This is consistent with previous reports in mammalian (Mayer et al. 2015; Jonkers et al. 2014) and *Drosophila* cells (Kwak et al. 2013). In addition, peak density is sharply increased around the 5' splice site (**Figure 4B**). This could indicate Pol II pausing associated with splice site recognition. However, we cannot exclude that the pattern could also be due to misalignment of splicing intermediate reads that should map to the final exonic nucleotide. The profile around the 3' splice site is more complex, with first an isolated high peak density region just after the 3' splice site, and then a drastic increase in average peak density starting roughly 60 nt after the 3' splice site (**Figure 4B**). It thus appears that Pol II elongation behaviour indeed covaries with the locations of exon-intron boundaries.

A potential caveat is that nucleotide composition varies systematically across exons and introns. For example, exons tend to have a higher GC content than introns (Zhu et al. 2009). This could be problematic as NET-seq relies on MNase digestion of DNA and RNA to solubilize chromatin. MNase digestion of DNA is known to be sequence-biased, with most notably a preference for cleaving just 5' of an adenine (Dingwall et al. 1981; Hörz and Altenburger 1981; Gaffney et al. 2012). An analysis of the 5' ends of our reads revealed similar biases for MNase digestion of RNA (**Figure 4D**). This sequence preference could lead to artefactual variation in read density, with more reads being sampled from transcripts and transcript regions whose nucleotide composition is more similar to MNase digestion biases. To verify to what extent our results were affected by this confound, we performed a simulation to determine the expected distribution of reads based on the digestion bias alone

(Supplementary Methods). We concluded that MNase biases are unlikely to explain either the enrichment of peaks in exons or the high peak densities observed just around the splice sites. However, it is possible that the exact location and size of the large peak starting ~60 nt into the exon is affected by the bias.

In conclusion, we detect both a general decrease in elongation rates over exons as well as pausing in the vicinity of the splice sites.

***d*NET-seq captures recursive splicing intermediates.**

Having shown that the spliceosome forms a complex with the elongating Pol II in *Drosophila* embryos and that Pol II pausing is correlated with position relative to the splice sites, we asked when splicing takes place relative to transcription. We first looked at recursive splicing of long introns because this process involves the formation of inherently unstable intermediates that are more likely to be formed soon after the transcription of each intronic splice site (Pai et al. 2018). In recursive splicing, long introns are removed by sequential excision of adjacent sections involving separate splicing reactions, each producing a distinct lariat (Hatton et al. 1998). Recursively spliced intron segments are bounded at one or both ends by recursive sites or ratchet points (Burnette et al. 2005), which correspond to zero nucleotide exons consisting of juxtaposed 3' and 5' splice sites around a central AG|GT motif, where the vertical line represents the splice junction (**Figure 5A**).

To capture recursive splicing intermediates using *d*NET-seq, it is essential to have a good coverage of reads corresponding to nascent transcripts and spanning the splice junctions. The total number of reads resulting from nascent RNA in each *d*NET-seq dataset is depicted in **Figure S1E**. By merging the sequencing information of overlapped paired-end reads (**Figure 1E**), we were able to sequence on average ~103 nucleotides per nascent RNA (**Figure S1D and S1F**). Focusing on previously identified *Drosophila* ratchet points (Joseph et al. 2018; Duff et al. 2015), we found *d*NET-seq/S5P reads that span the junction between the canonical 5' splice site at the end of the exon and the first ratchet point (RP1) internal to the downstream intron, as shown for the second intron of the *Megalin* gene (**Figure 5B**). Reads spanning the subsequent intronic RPs were also observed (**Figure 5B**).

Overall, we detected *d*NET-seq/S5P and *d*NET-seq/S2P spliced reads supporting most of the previously identified recursive splicing events (**Figure 5C and S5A**).

Analysis of *d*NET-seq profiles around a RP reveals an enrichment of reads in a region located a few nucleotides downstream of the RP, as shown for RP2 in the first intron of the *Tenascin major* gene (**Figure 5D**). Noteworthy, most of these reads are already spliced to the previous RP (**Figure 5D**). A meta-analysis of *d*NET-seq/S5P reads around 137 RPs confirms that many spliced reads can be observed just downstream of RPs **(Figure 5E, F)**. Taken together, these results indicate that recursive splicing can occur soon after the transcription of intronic recursive sites and suggest the presence of paused Pol II downstream of these sites.

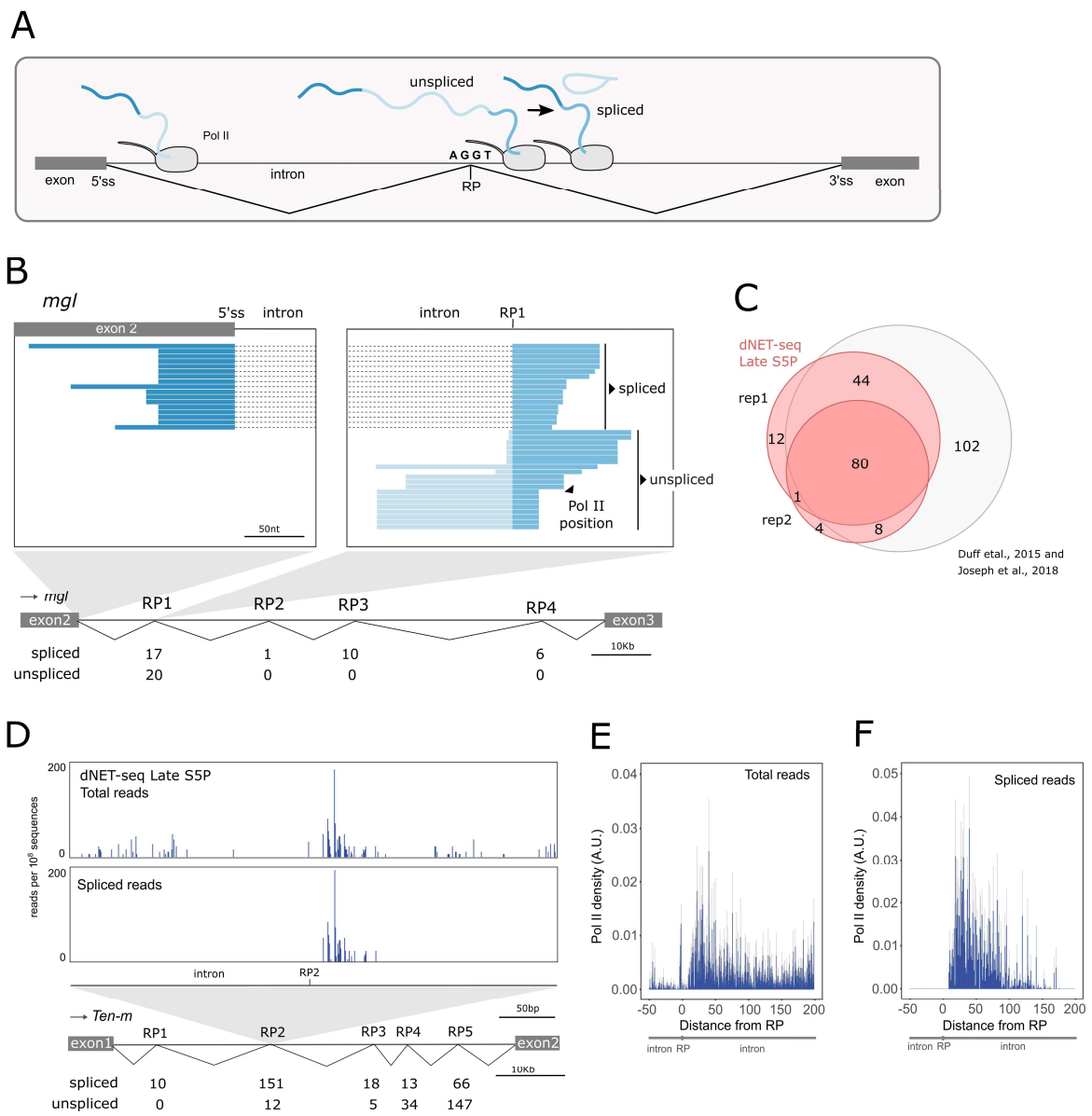

Figure 5. *d*NET-seq captures recursive splicing intermediates. (A) Schematic illustrating recursive splicing. A ratchet point (RP) with juxtaposed acceptor and donor splice site motifs is indicated. **(B)** Visualization of *d*NET-seq/S5P reads that align to the second intron of the *Megalin* (*mgl*) gene. Recursively spliced reads align to exon 2 (green) and the intron after RP1 (dark red). The number of spliced and unspliced reads at each RP in the intron is indicated. **(C)** Venn diagram comparing RPs identified in two *d*NET-seq/S5P biological replicates and in previously reported studies (Joseph et al. 2018; Duff et al. 2015). **(D)** Number of *d*NET-seq/S5P reads that have the 3' end mapped around RP2 in the first intron of *Tenascin major* (*Ten-m*) gene. The top panel depicts all reads, and the bottom panel depicts only reads that have been spliced to RP1. **(E-F)** Meta-analysis with single nucleotide resolution of normalized *d*NET-seq/S5P reads around RPs (n=137) using all reads **(E)** or only reads spliced to the previous RP or exon **(F).**

Splicing takes place as Pol II transcribes past the 3' splice site, yet many nascent transcripts remain unspliced.

Reads that span exon-exon junctions corresponding to spliced nascent transcripts were found in both *d*NET-seq/S5P and *d*NET-seq/S2P libraries prepared from early and late embryos **(Figure 6A)**. To identify which splicing events were detected by *d*NET-seq, we considered all internal and fully-coding exons that are at least 100 nt long in actively transcribed genes. For each splice junction, we counted how many reads had the 3' end mapped to the first 100 nt of the exon. Only exons with at least 10 reads mapping to this region were considered (see the methods section for justification of the threshold). Then, the *d*NET-seq splicing ratio (SR) was calculated by dividing the number of spliced reads by the sum of the number of spliced and unspliced reads **(Figure 6A).** Reads could be counted as spliced or unspliced if their 3' end mapped to within the first 100 nt of the exon and their 5' end reached upstream of the 3' splice site, allowing to check whether the intron was still present. A robust agreement of estimated SRs was observed between biological replicates for pre-MBT genes (**Figure S6A**) and genes expressed in late embryos (**Figure 6B**).

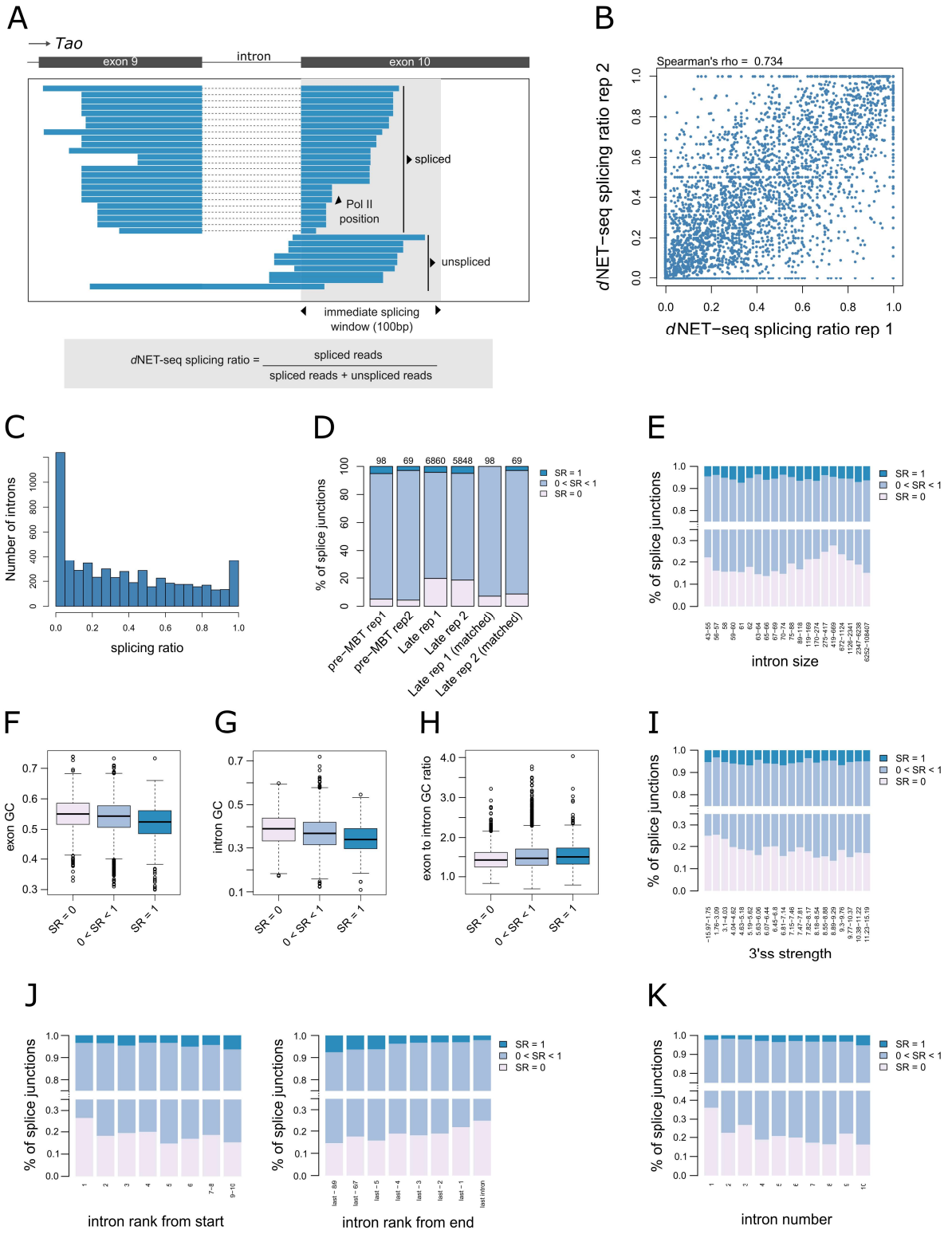

Figure 6. Splicing occurs as Pol II transcribes past the 3' splice site.

(A) Visualization of *d*NET-seq/S5P reads that align to exon 10 of the *Tao* gene. For **(B-J)**, unless otherwise specified, only introns from transcriptionally active genes where the downstream exon is a fully coding internal exon at least 100 nt long were included. In addition, enough spliced/unspliced reads had to end within the first 100 exonic nucleotides that obtaining a splicing ratio (SR) of 0 or 1 by chance alone was highly unlikely (see the methods section for details). For genes expressed in late

embryos, this threshold was 10 reads for both replicates. For pre-MBT genes, it was 14 for replicate 1 and 9 for replicate 2. **(B)** Values of *d*NET-seq SRs estimated in two biological replicates of *d*NET-seq/S5P datasets from late embryos (Spearman correlation, $\rho = \sim 0.734$, $P < 2.2 * 10^{-16}$; N = 3708). **(C)** Histogram of SRs for *d*NET-seq/S5P. N = 5626. **(D)** Splice junctions in pre-MBT genes and genes expressed in late embryos classified according to their *d*NET-seq splicing ratio. As many pre-MBT genes are single-intron, last introns were exceptionally included in this analysis. To make the two columns on the right, we used a subset of the genes expressed in late embryos (post-MBT genes) that was as similar as possible to the pre-MBT set in read number. Concretely, to match each pre-MBT gene, we picked the post-MBT gene that had the most similar total count of spliced and unspliced reads, making sure that every post-MBT gene only appeared in the subset once. **(E-K)** Several parameters of gene architecture show a relationship with SR. For the sample sizes and statistical tests used, see **Supplementary Table 1**. Note that in **(E, I-K)**, the bin ranges have been set so that intron numbers would be as equal as possible between bins. ss: splice site.

SRs showed a bimodal distribution, with peaks at both extremes (SR = 0 and SR = 1; **Figures 6C** and **S6B**). Hence, for the remainder of the analysis, we performed all comparisons between three discrete SR classes (SR = 0, 0 < SR < 1, and SR = 1). We observed that only ~5% of splice junctions in pre-MBT genes were devoid of reads spanning ligated exons and thus presented an SR of 0 (~5.10% replicate 1/~4.35% replicate 2), whereas in genes expressed in late embryos this proportion was ~20% (~19.72% replicate 1/~18.55% replicate 2) (**Figure 6D**; two-tailed binomial test for difference between late and pre-MBT, $P \sim 6.141 * 10^{-5}/9.44 * 10^{-4}$ (replicate 1/replicate 2)). However, this difference between pre-MBT genes and genes expressed in late embryos disappeared once the higher read density of pre-MBT genes had been controlled for (**Figure 6D**).

Thus, in most cases, *Drosophila* co-transcriptional splicing can occur when Pol II is still transcribing the downstream exon, implying an intron definition mechanism as previously proposed for *S. cerevisiae* (Carrillo Oesterreich et al. 2016). Consistent with this view, many *Drosophila* transcripts have relatively long exons separated by short introns – a gene architecture suggested to be conducive to intron definition. Very long introns flanked by short exons have instead been associated with exon definition (under which the downstream exon needs to be fully transcribed before splicing can take place) (Keren et al. 2010). A switch to exon definition was proposed once the size of the intron surpasses ~200 nt (Fox-Walsh et al. (2005). It is unclear, however, whether the choice between exon and intron definition is dependent on the absolute sizes of exons and introns, or rather the ratio of intron to exon size.

We found no relationship between the *d*NET-seq splicing ratio and exon length (**Figure S6C, G** for replicates 1 and 2; see **Supplementary Table 1** for details on statistical significance and sample sizes for all of the gene architecture parameters discussed here). Regarding intron size, we found that introns with SR = 0 (and thus no evidence for intron definition) were, on average, indeed larger than other introns (**Figures 6E** and **S6F**). However, more careful examination revealed a more complex picture, with a lower proportion of introns with SR = 0 both for introns of intermediate size (~55-100 nt, which corresponds to ~55% of the introns studied) and for very large introns (>1000 nt) (**Figure 6E**). These intron sizes may thus be optimal for fast splicing. We also uncovered a lower exon to intron length ratio for introns with SR = 0 than for others (**Figure S6D, H**; although note that effect was near-significant for replicate 1).

Taken together, these results suggest that although fast splicing (implying intron definition) is indeed skewed towards small introns flanked by large exons, there is also frequent and efficient intron definition for large introns. Our results are inconsistent with a threshold model, where splicing would systematically switch to exon definition after a given intron size is reached.

We also investigated the relationship between SR and several other gene architecture parameters. Firstly, as the GC content in exons and introns decreases, the proportion of introns with SR = 1 increases and the proportion with SR = 0 decreases, showing more efficient immediate splicing (**Figures 6F, G** and **S6J, K**). A similar effect is observed as the ratio of the downstream exon GC content to intron GC content increases (**Figures 6H** and **S6L**). Thus, the most efficient immediate splicing is observed when the GC content is low in both exons and introns but higher in exons than introns. Secondly, similarly to previous reports (Khodor et al. 2011, 2012; Herzel et al. 2018), we uncovered an effect of exon rank, whereby exons that are more central appear to be spliced more efficiently (**Figures 6J** and **S6N**). Thirdly, as 3' splice site strength increases, the proportion of introns with SR = 0 decreases (**Figures 6I** and **S6M**). We found no significant relationship between SR and 5' splice site strength (**Figure S6E, I**). Finally, as previously observed (Khodor et al. 2012), transcripts with only a single intron tend to be spliced less efficiently than multi-intron ones, with a higher proportion of SR = 0 introns (**Figures 6K** and **S6O**).

In conclusion, *d*NET-seq reveals that splicing can occur as Pol II transcribes past the 3' splice site, yet many nascent transcripts remain unspliced.

Pol II pausing is associated with co-transcriptional splicing.

Analysis of individual *d*NET-seq profiles around constitutive splice junctions with a high splicing ratio frequently revealed an enrichment of reads downstream of the 3' splice site, coincident with the appearance of spliced reads, as shown for the *cno* gene (**Figure 7A**). In contrast, profiles around a constitutive splice junction with SR = 0 had an accumulation of reads further along the exon, as shown for the *ND-51* gene (**Figure 7B**). A clearly distinct type of profile was observed on skipped exons, on which very few reads were observed, as shown for the *zip* gene (**Figure 7C**).

We next performed a meta-analysis of NET-seq peak densities over different exonic and intronic regions (**Figure 7D-F**). Introns with SR = 1 displayed a characteristic Pol II peak density profile, with a single region of high density ~10-20 nucleotides after the 3' splice site (**Figure 7F**). This profile was strikingly different from introns with lower SR values, which showed two high density regions: a small and narrow peak immediately after the 3' splice site and a broader and higher peak starting ~60 nucleotides into the exon (**Figure 7D-E**). We attempted a separate meta-analysis of skipped exons. These exons showed no accumulation of Pol II. However, the sample size was too small for meaningful comparisons with included exons.

Taken together, these results indicate that, as observed for recursive splicing, Pol II pauses soon after the 3' splice site when the splicing reaction is completed at that position. When no immediate splicing is detected by *d*NET-seq on constitutively spliced exons, Pol II pausing is still observed but it starts further away from the 3' splice site, suggesting that splicing may occur as Pol II reaches that position. It is unclear how to interpret the small increase in peak density immediately after the 3' splice site for introns with SR = 0.

Finally, we asked how prevalent co-transcriptional splicing is in the developing *Drosophila* embryo. As shown in **Figure 2E**, approximately 80% of exons in pre-MBT genes and genes expressed in late embryos covered by a high density of NET-seq reads have a peak corresponding to the splicing

intermediate formed after cleavage at the 5' splice site but before exon-exon ligation. The majority of these exons (~85%) were covered by *d*NET-seq reads that span the junction to the downstream exon either directly on nascent transcripts or indirectly on splicing intermediates formed by cleavage at the 5' splice site of the downstream exon **(Figure 7G, I)**, confirming that they are co-transcriptionally spliced. We then focused on those exons for which no splicing intermediate spike was detected by the peak calling algorithm, as illustrated for the *Doc3* gene **(Figure 7H, J)**. Over 71% of these exons were also covered by *d*NET-seq reads that span the junction to the downstream exon either directly on nascent transcripts or indirectly on splicing intermediates formed by cleavage at the 5' splice site of the downstream exon **(Figure 7J)**, arguing that even exons without a detectable splicing intermediate peak are co-transcriptionally spliced. Altogether, our *d*NET-seq results support co-transcriptional splicing for over 95% of the analysed exons.

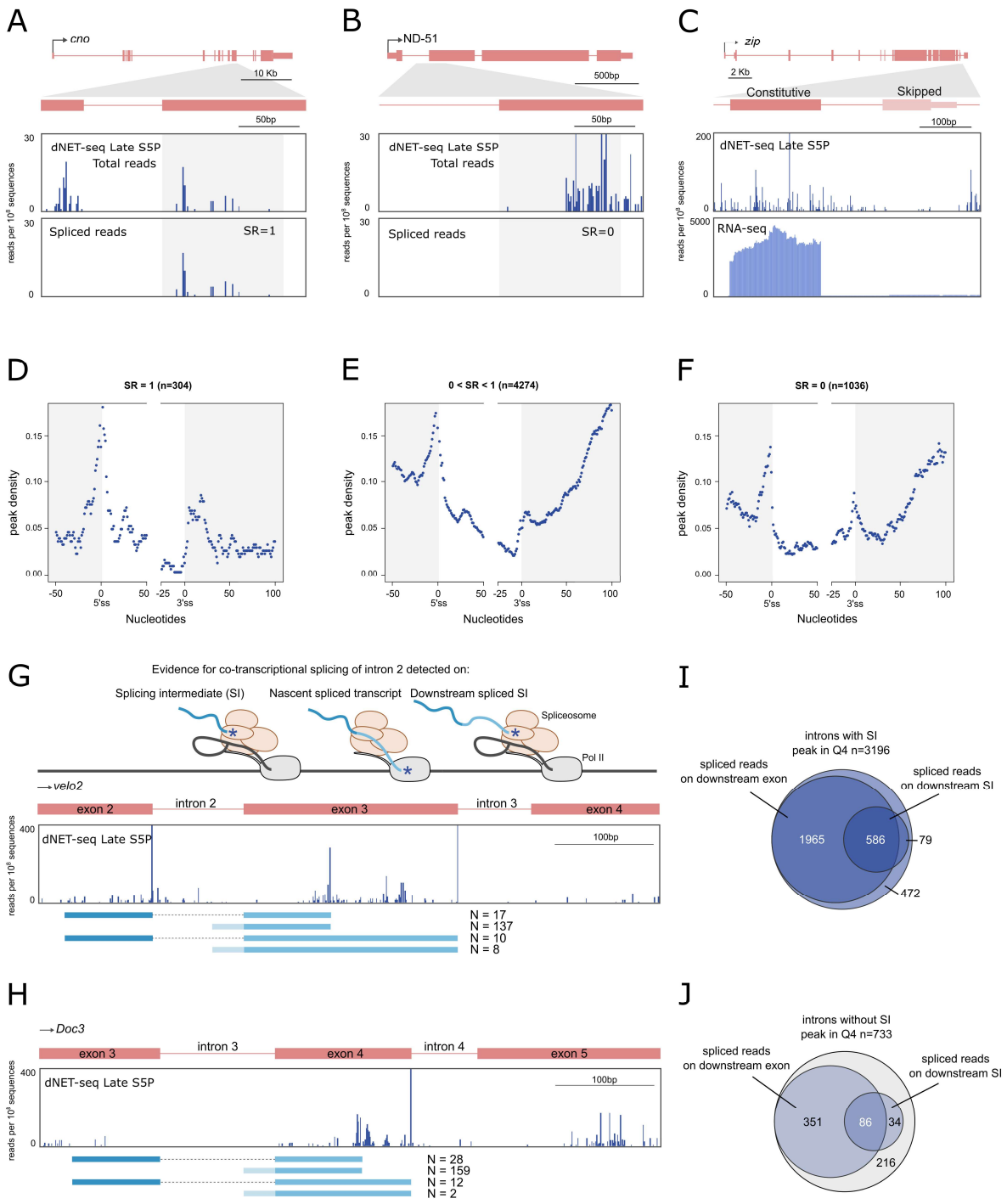

Figure 7. Pol II pausing is associated with co-transcriptional splicing.
(A-C) *d*NET-seq/S5P profiles surrounding the indicated exons in the post-MBT genes *cno* (**A**), *ND-51* (**B**), and *zip* (**C**). The top panels depict all reads. The bottom panels depict either the 3' end coordinate of reads that span the splice junction **(A, B)**, or the RNA-seq profile (**C**). **(D-F)** Metagene analysis of Pol II peak density estimated from *d*NET-seq/S5P datasets from late embryos (replicate 1). Peak density has been calculated as the proportion of introns that overlap with a peak at any given position. The last 50 nucleotides of exons, the first 50 nucleotides of introns, the last 25 nucleotides of introns, and the first 100 nucleotides of exons are shown. Only internal and fully coding exons from transcriptionally active genes that are at least 100 nucleotides long are shown. In addition, at least 10 spliced/unspliced reads had to end within the first 100 nucleotides of the exon. The introns have been split between SR = 0 **(D)**, 0 < SR < 1 **(E)** and SR = 1 **(F)**. **(G-H)** *d*NET-seq/S5P profiles on the indicated regions of the

velo2 and *Doc3* genes. Below, spliced reads are depicted. Asterisks denote the splicing intermediate peaks at the end of exons. **(I-J)** Venn diagrams showing how many junctions with or without a splicing intermediate peak are covered by spliced reads or have a downstream splicing intermediate covered by spliced reads.

DISCUSSION

In this study, we used *d*NET-seq to map Pol II over the bodies of genes that become transcriptionally active in *Drosophila* embryos during the initial stages of development. The use of embryos allowed us to perform an important test to verify that the captured RNA is truly nascent. Indeed, early *Drosophila* embryos contain abundant mRNAs that are transcribed during oogenesis and loaded into the egg. In our analysis of early embryos, these maternal transcripts were readily detected by RNA-seq, but not by *d*NET-seq.

Embryonic development in *Drosophila* starts with 13 rapid mitotic cycles with a duration of approximately 10 minutes (Ji et al. 2004). Subsequent cycles become longer, with cycle 13 taking about 21 minutes and cycle 14 lasting for at least 65 minutes. The abruptly extended cycle 14 is marked by the massive activation of zygotic transcription, as the embryo switches from relying on maternally deposited mRNAs and proteins to undergoing its own transcription (Tadros and Lipshitz 2009; Yuan et al. 2016). However, the onset of zygotic genome activation in *Drosophila* begins in cycle 8 for a few genes (Erickson and Cline 1993; Pritchard and Schubiger 1996) and then the number of active genes gradually increases until cycle 14 (Kwasnieski et al. 2019). Genes that are transcriptionally active before the end of cycle 13, i.e., before the mid-blastula transition (MBT), are called pre-MBT genes. Of note, transcriptional activation is a continuous process, with nearly all genes activated before MBT remaining transcribed later (Kwasnieski et al. 2019).

Transcription in the *Drosophila* early embryo is restricted to interphase (Shermoen and O'Farrell 1991) and proceeds at a rate of 2.4-3.0 kb per minute (Fukaya et al. 2017). Given the short length of the initial interphases, there are significant constraints to pre-MBT transcription and splicing. Although pre-MBT genes are on average shorter than the overall genes expressed at later stages of development (Artieri and Fraser 2014; Hoskins et al. 2011), longer genes are nevertheless transcribed before MBT. However, before cycle 14 transcriptional elongation of long genes is either prematurely terminated (Sandler et al. 2018) or aborted (Shermoen and O'Farrell 1991; Kwasnieski et al. 2019). It has also been reported that pre-MBT expression is associated with the generation of DNA damage due to stalling of DNA replication at transcriptionally engaged loci (Blythe and Wieschaus 2015b).

Our *d*NET-seq analysis revealed a novel feature of pre-MBT genes that most likely contributes to reduce conflicts between transcription and replication during the short interphases of early embryos. We found that in the majority of pre-MBT genes, transcription is efficiently terminated at the TES, whereas many of the genes that are only expressed after MBT show high *d*NET-seq signal past the TES. We also observed that most pre-MBT genes are isolated from other transcriptional units, while the TES of many post-MBT genes is overlapped by another gene transcribed in the opposite direction, suggesting that *Drosophila* genome architecture is also under selection for efficient pre-MBT gene expression and avoidance of DNA damage. Whether there is a mechanistic link between transcriptional read through and the presence of an overlapping convergent gene remains to be determined. Clearly, further studies are needed to understand how transcription termination is regulated in the early *Drosophila* embryo.

A classical view in the splicing field is that for some introns, the 5' and 3' splice sites are recognized directly by 'intron definition'. For other introns, spliceosome assembly starts with the recognition of the downstream exon, and only at a later stage a cross-intron complex is formed ('exon definition') (Robberson et al. 1990; Berget 1995; Sterner et al. 1996; Fox-Walsh et al. 2005). These alternative models are supported by *in vitro* evidence, as well as by *in vivo* reporter gene experiments (Robberson et al. 1990; Berget 1995; Fox-Walsh et al. 2005; De Conti et al. 2013). There is also indirect evidence, for example from analysis of exon-intron size patterns (Berget 1995). However, these models have never been directly tested *in vivo* at transcriptome-wide level. It thus remains uncertain how intron definition and exon definition operate *in vivo* and what determines the choice between them.

Introns that show splicing completion before Pol II has reached the end of the downstream exon are necessarily intron-defined, as exon definition requires the presence of the 5' splice site of the downstream intron. Therefore, introns with an SR above 0 represent an experimentally-determined set of introns that are spliced *via* intron definition at least part of the time, allowing us to test long-held assumptions in the field. Notably, *in vitro* and reporter gene work suggested that *Drosophila* uses intron definition for introns smaller than ~200-250 nt and exon definition for larger introns (Fox-Walsh et al. 2005). Other studies have suggested that the crucial factor is not just intron size but the relative size of the intron compared to the flanking exons (Sterner et al. 1996).

Using *d*NET-seq, we have found that although there is a relationship between intron size and the proportion of introns with SR > 0, intron definition can be observed at all intron sizes. Our results are thus inconsistent with a simple "threshold" model, where splicing would systematically switch to exon definition at a particular intron size. Rather, we observe an increased proportion of introns with SR > 0 within an optimal intron size range of ~55-100 nt. The median intron size in our data set is 71 nt. It thus appears that intron definition is best optimized for introns of a "typical" size, and is less efficient when introns are unusually small or large. Intriguingly, however, for very large introns (>1000 nt), the proportion with SR > 0 increases again, suggesting that specific mechanisms may have evolved for the intron-defined splicing of very large introns. The tendency for faster splicing kinetics with average intron sizes has also been reported using metabolic labelling in both *Drosophila* (Pai et al. 2017) and human cells (Windhager et al. 2012).

We propose that the tethering of the upstream exon to Pol II (de Almeida and Carmo-Fonseca 2008) could be crucial for the intron-defined splicing of such large introns. Indeed, introns with SR > 0 where the upstream exon has one or more putative splicing intermediate reads tend to be larger than ones without splicing intermediate reads (one-tailed Mann-Whitney *U*-test, W = 779623, P ~ 0.003, N = 4589; exon size and read number filtering has been applied like for the gene architecture analysis).

In addition, Pai et al. (2017) found that GC poorer introns were spliced faster. We uncovered a similar relationship with GC content, with the highest proportion of introns with SR > 0 observed when both the exon and the intron were AT-rich but the exon had a higher GC content than the intron. We emphasize that the gene architecture parameters that we have investigated are not independent of each-other. For instance, exon GC content is correlated negatively with exon rank from start (Spearman's $\rho \sim -0.098$; $P \sim 1.196 * 10^{-12}$). Further work is thus needed to distinguish between causative and merely correlative factors. In addition, it must be determined how the GC content effect relates to patterns of nucleosome density (Gelfman et al. 2013).

Our results indicate that the majority (>80%, based on the data set used in **Figure 7 D-F**) of *Drosophila* introns expressed in late embryos can be spliced through intron definition. Among these introns, a discrete subset show evidence of being spliced as soon as the 3' splice site has been transcribed, associated with a Pol II pause at the start of the exon. For other intron-defined introns, Pol

II pausing is also observed but later in the exon. In yeast, Harlen et al. (Harlen et al. 2016) observed an exon-start peak very similar to that reported here, and found that it was particularly associated to exons with high levels of U1 occupancy.

An important caveat of our work is that introns that show no evidence for splicing completion during transcription of the downstream exon could still be spliced *via* intron definition, if their splicing takes too long for it to be detected during the 100 nt window studied. Therefore, we do not know whether introns with a SR of 0 are exon-defined, intron-defined but spliced when Pol II has elongated past the first 100 exonic nucleotides, or a mixture of both. Similarly, introns with a splicing ratio between 0 and 1 could either always be intron-defined, or they could use either exon or intron definition depending on the splicing event.

Finally, it is important to highlight that while only a minority of splice junctions were devoid of reads spanning ligated exons (corresponding to an SR of 0), many introns remained unspliced in our analysis. Given the size limit of *d*NET-seq reads, it is not possible to define the timing of splicing of these introns. Yet, our results reveal at unprecedented level a complex range of heterogeneity in splicing dynamics. Why is any particular intron either excised shortly after Pol II transcribes the 3' splice site or left unspliced while the transcript elongates? Is this a stochastic process? What are the consequences for gene expression of fast versus delayed splicing? Addressing these questions will require further advances in methodologies to study splicing in time and space at a transcriptome-wide level.

METHODS

Embryo collection

Drosophila melanogaster flies (Oregon R (OrR) strain) were raised at 25°C, in polypropylene vials containing standard enriched culture medium (cornmeal, molasses, yeast, soya flour, and beetroot syrup). Three-day-old flies (counting from pupae eclosion) were fattened in culture medium supplemented with fresh yeast for 2 days. Embryos were collected into apple juice-agar plates supplemented with fresh yeast using appropriate cages containing approximately 200 flies each. To

avoid female retention of older embryos, three pre-collections of 30min each were made before the first collection of embryos. To maximize egg laying, and avoid larvae contamination, adult flies were transferred to clean embryo collection cages every day over five days. For early stage embryos (2-3 hours after egg-laying), adult females were allowed to lay eggs for 1 hour in apple juice-agar plates. Plates were subsequently collected and embryos were aged at 25°C for 90 min. During the following 30 min, embryos were harvested from the plates, dechorionated in 50% bleach solution for 2 min, and washed once in Phosphate Buffered Saline supplemented with 0.1% Tween-20 (PBT) and twice in deionized water. In order to discard older embryos (stage 6 and older), manual staging of collected embryos was performed with the help of forceps and under a magnifier scope. Embryos were then resuspended in a solution containing 120mM NaCl and 0.04% Triton, and washed twice with 120mM NaCl solution. At the end of the 3 hours collection, the solution was removed and embryos were frozen in liquid nitrogen and stored at -80ºC. For the late stage (4-6 hours), eggs were laid for 2 hours and aged at 25°C for 3.5 hours. Embryo collection and processing was similar to the early stage embryos, but in this case, no manual staging was performed.

Embryo DNA staining

For each embryo collection, and after dechorionation, a representative embryo sample was collected from the total pool and fixed in a scintillation flask, using a solution containing 1 volume of 4% formaldehyde in PBT and 4 volumes of heptane, for 20 min at 100rpm. The lower aqueous phase solution was subsequently removed, 4ml of methanol was added and embryos were shaken vigorously during 1 min. Embryos were then collected from the bottom of the scintillation flask, washed twice with methanol, and frozen at -20ºC in methanol. To rehydrate the embryos, they were washed for 5 min each, with 3:1, 1:1, and 1:3 mix solutions of methanol:PBT. Embryos were subsequently washed twice in PBT and incubated with 1:5000 Sytox green (Invitrogen), supplemented with 5µg/ml RNase A (Sigma-Aldrich) in PBT for 15 min. After washing with PBT, embryos were mounted in fluorescence mounting medium (Dako) and examined in a Zeiss AxioZoom V16 Fluorescence Stereo Microscope for image acquisition and embryo staging. Images were processed using ImageJ software (NIH).

***d*NET-seq and library preparation**

The *d*NET-seq protocol was adapted from mNET-seq (Nojima et al. 2016). Briefly, 300 ul of frozen embryos was resuspended in 3.5ml of Buffer B1 (15mM HEPES-KOH, pH 7.6; 10mM KCl; 5mM MgCl2; 1mM DTT; 0.1mM EDTA; 0.35M Sucrose; 4µg/ml Pepstatin; 10mM Sodium Metabisulfite; 0.5mM EGTA supplemented with complete EDTA free protease inhibitor (Roche) and PhoSTOP (Roche)). Embryos were homogenised in a Dounce homogenizer with 11x strokes using a tight pestle on ice. The suspension was centrifuged at 7700g for 15 min at 4ºC, the supernatant was discarded and the white pellet containing the nuclei was resuspended in 500 µl of Buffer B1. The suspension was again homogenised in the Dounce with 4x strokes and loaded without mixing on the top of buffer B2 (15mM HEPES-KOH, pH 7.6; 10mM KCl; 5mM MgCl2; 1mM DTT; 0.1mM EDTA; 0.8M Sucrose; 4µg/ml Pepstatin; 10mM Sodium Metabisulfite; 0.5mM EGTA supplemented with complete EDTA free protease inhibitor (Roche) and PhosSTOP (Roche)). The suspension was centrifuged at 1310g during 30 min at 4ºC, and the pellet was resuspended with 125 µl of NUN1 buffer (20mM Tris-HCl (pH 7.9); 75 mM NaCl; 0.5mM EDTA and 50% Glycerol). 1.2ml of Buffer NUN2 (300mM NaCl, 7.5mM MgCl2, 1% NP-40, 1M Urea supplemented with complete EDTA free protease inhibitor (Roche) and PhoSTOP (Roche) was mixed with the nuclei and incubated on ice during 15 min preforming short vortex every 3 min. Chromatin was then centrifuged at 10000g for 10 min at 4ºC, washed with 100 µl of 1x MNase Buffer and incubated in 100µl of MNase reaction mix (1x MNase buffer and 30 gel unit/µl MNase (New England Biolabs)) during 3 min at 37ºC with mix at 1400rpm. The reaction was stopped with 10 µl of 250mM EGTA, centrifuged at 10000g for 5 min at 4ºC, and the supernatant containing the solubilized chromatin was recovered. For the early embryos sample, 2x 300µl of embryos were prepared in parallel and pooled together after the chromatin solubilization. Immunoprecipitation of Pol II-RNA complexes was performed using 50µl of Protein G Dynabeads (Thermo Fisher Scientific), pre-incubated over night with 5µg of the correspondent antibody: anti-Pol II CTD S5P (ab5131 Abcam) or anti-Pol II CTD S2P (ab5095 Abcam) in 100µl NET2 (50mM Tris-HCl pH 7.4; 150mM NaCl and 0.05% NP-40) and washed 3 times with NET2. Beads were incubated

with the solubilized chromatin in 1ml total volume of NET2 during 1 hour at 4ºC, washed 7 times with 500µl of NET2 and once with 100µl of PNKT (1x PNK buffer and 0.1% tween) before incubation during 6 min in 50µl of PNK reaction mix (1x PNKT, 1 mM ATP and 0.05 U/ml T4 PNK 3′phosphatase minus (NEB) in a thermomixer at 37ºC and 1400rpm. After washing the beads with NET2, long RNA fragments were isolated using Quick-RNA MicroPrep (Zymo research): 300µl of RNA Lysis Buffer in 33% EtOH was mixed to the beads by pipetting. Beads were discarded and the suspension was loaded into a Zymo spin column that was centrifuged at 10000g during 30sec. The column was washed once with 400µl RNA prep buffer and twice with 700µl and 400µl RNA wash buffer respectively. RNA was then eluted in 15µl of DNase/RNase-Free water (zymo) and stored at -80ºC. 100ng of RNA was used to prepare each library, following the standard protocol of the Truseq small RNA library prep kit (Illumina). After adapter ligation and reverse transcription, the libraries were PCR amplified using 16 PCR cycles and cDNA libraries were fractionated in the gel between 130 to 300bp. The libraries were sequenced using PE-150 on the Illumina HiSeq X platform by Novogene Co., Ltd.

QUANTIFICATION AND STATISTICAL ANALYSIS

*d*NET-seq data processing

Adapter sequences were removed from all *d*NET-seq paired-end samples using Cutadapt (version 1.18) (Martin 2011) with the following parameters: -a TGGAATTCTCGGGTGCCAAGG -A GATCGTCGGACTGTAGAACTCTGAAC -m 10 -e 0.05 --match-read-wildcards -n 1. Paired-end read merging was performed using bbmerge.sh from BBMap (Bushnell et al. 2017) with the 'xloose' parameter. Merged reads were then aligned to the *Drosophila* reference genome (*dm6*; Ensembl release 95) (Cunningham et al. 2019) using STAR (version 2.6.0b) (Dobin et al. 2013) with –chimSegmentMin set to 20. Only uniquely mapped reads were considered, extracted using SAMtools (version 1.7) (Li et al. 2009) with -q set to 255. Exceptionally, in **Figure S2A**, HiSat2 was used, using the same dm6 genome annotation file for genome indexing and using default parameters, with the --no-discordant –no-mixed flags set. PCR internal priming events generated during library preparation were removed using a custom Python script (Prudêncio et al. 2020) with the following parameters: -a TGG.. -s paired.

To obtain single-nucleotide resolution, a custom Python script (Prudêncio et al. 2020) was used to extract the 5' end nucleotide of read 2 (after trimming) in each sequencing pair, with the directionality indicated by read 1 (**Figure 1E**).

Publicly available RNA-seq datasets used

Publicly available *Drosophila* embryonic transcriptome sequencing data (Poly(A) RNA-seq), performed in developmental stages similar to the dNET-seq early and late samples, were used in this study. RNA-seq datasets corresponding to cycle 14B (Lott et al. 2011) were obtained from the Gene Expression Omnibus (GEO) (samples GSM618409, GSM618410, GSM618421 and GSM618422 from dataset GSE25180). RNA-seq datasets from 4-6h old embryos were obtained from modENCODE project PRJNA75285 (Graveley et al. 2011) (accessions SRR023696, SRR023746, SRR023836, SRR035220, SRR023669, SRR035405, SRR035406, SRR024014 and SRR023539).

RNA-seq data processing

Adapters were removed from all datasets using Trim Galore (version 0.4.4) (http://www.bioinformatics.babraham.ac.uk/projects/trim_galore/; last accessed 26 April 2020). Datasets from modENCODE and GEO were aligned to the *dm6 Drosophila* reference genome (Ensembl release 95) (Cunningham et al. 2019) using STAR (version 2.6.0b) (Dobin et al. 2013) with --chimSegmentMin set to 20. Stringtie (version 1.3.3b) (Pertea et al. 2015) was used to quantify normalized gene expression as Transcripts Per Kilobase Million (TPM) values with the following parameters: -a 5 -e. In addition, the isoform list was provided together with the -G parameter corresponding to the *dm6* (Ensembl release 95) GTF file. Genes with TPM values above 2 were considered to be expressed.

Selection of genes and isoforms for analysis

Similar to a previous GRO-seq analysis (Core et al. 2008), we used the read density of very large intergenic regions (gene desert regions) to define the reference for absence of transcription. Gene deserts were divided into 50kb windows, and *d*NET-seq read densities were calculated by dividing the read counts in each window by the window length (in bp). Read counts per window were obtained with bedtools genome coverage (version 2.27.1-1-gb87c465) (Quinlan and Hall 2010), and an arbitrary density threshold was defined as the 90th percentile of the read density distribution (**Figure S4A**). Transcripts whose gene body *d*NETseq read density exceeded this threshold were considered to be transcriptionally active. (**Figure S4B**). For all of the analyses performed on late genes, only transcriptionally active genes were considered. In addition, only one isoform per gene was considered for all analysis, selected as the isoform with the highest RPKM value in the RNA-seq dataset for the corresponding developmental stage.

The coordinates of previously identified pre-MBT genes were obtained from Chen et al. (2013) and converted to *dm6* coordinates using the *liftOver* tool (https://genome.ucsc.edu/cgi-bin/hgLiftOver). The most representative isoform for each gene was manually selected through visualization of individual profiles.

Splicing intermediate and lariat detection

Exons containing splicing intermediates or introns containing lariats were identified using a peak finder algorithm (NET_snrPeakFinder) (Churchman and Weissman 2011; Prudêncio et al. 2020) that detects the presence of a peak in the last nucleotide of an exon (splicing intermediate) or an intron (lariat), by comparing the accumulation of 3' end reads mapping at that position with the mean read density of the flanking 200 nucleotides. A peak is called when the read density at the peak is superior to the mean of this surrounding region plus 3 standard deviations (Churchman and Weissman 2011). Since gene read density influences peak detection, the exons were divided into quartiles based on the *d*NET-seq read density of the corresponding gene. Only exons from the highest quartile (i.e. from genes with the highest read density) were considered in **Figure 2** for *d*NET-seq Late analysis.

Analysis of read density and peak calling

RPKM values for the merged *d*NET-seq datasets were calculated in the following manner:

$$RPKM\ (transcript) = \frac{\text{reads} * \ 10^4 * \ 10^6}{(\text{total uniquely mapped reads}) * (gene\ length\ in\ bp)}$$

Where 10^4 normalizes for gene length and 10^6 normalizes for sequencing depth. Queries of gene 3'UTR overlaps (**Figure 3**) between genes were performed with bedtools intersect (version 2.27.1-1-gb87c465) (Quinlan and Hall 2010).

To detect splicing intermediate and intron lariat peaks, the algorithm from Churchman and Weissman (2011) was adapted as described in Prudêncio et al. (2020). To be able to call larger regions as peaks, a custom algorithm was developed and implemented in Python 3.7 (note that like for all of the custom Python code reported here, there is heavy reliance on *bedtools* v2.29.0 (Quinlan and Hall 2010) for operations on coordinate intervals). Our peak caller detects regions where the local read density is significantly higher than expected by chance given the overall read density of the transcript. Almost all of the numerical parameters used by the peak caller can be adjusted. In **Figure 4A**, results obtained with two particular parameterizations are shown. Peak Caller 1 ("large peaks") is adapted to detecting larger peaks and provides results that are more intuitive to a human observer. Peak Caller 2 ("small peaks") provides a finer spatial resolution, and corresponds to the settings used in all of the analyses in this study. The peak caller takes as input a BED file with the 3' ends of reads (single-nucleotide resolution), as well as a GTF file with transcript and exon annotations and a list of transcripts to analyse. It functions by calculating a sliding average of read density within each transcript (window size 5/21 for small/large; only reads mapping to the same strand as the annotated transcript are considered). It then randomly shuffles the positions of the reads within the transcript and recalculates the sliding averages to determine the random expectation. This can be repeated several times (5 in this study) for more robustness. Windows obtained with the true read distribution are called as significant if their read density is higher than the 99th percentile of the simulated windows. Note that in this study, we used a setting whereby this threshold is calculated separately for each exon (and its upstream intron,

for exons other than the first), by excluding the intron-exon pair of interest and reads overlapping it during the simulation step. This is necessary so that when calling peaks within a given exon (and its upstream intron), the threshold set would not be affected by the reads within that particular exon and its upstream intron. This way, for instance, the calling of a peak in the beginning of the exon is not affected by the calling of a peak in the middle of the same exon (except through potential merging, see below). After the initial peaks are called, they are filtered to remove peaks where more than 90% of the reads come from a single nucleotide (probable PCR duplicates), that are shorter than 5 nucleotides, or that overlap with fewer reads than a specified threshold (10/5 for large/small). Finally, peaks that are within a specified distance of each-other (21/5 nucleotides for large/small) are merged together.

Individual gene profiles

Individual dNET-seq gene profiles were generated by separating reads by strand using SAMtools (version 1.7) (Li et al. 2009). Strand-separated read data was converted to bedGraph format using bedtools genomecov with the -bg flag (version 2.27.1-1-gb87c465) (Quinlan and Hall 2010). Coverage values were normalized per nucleotide accounting for the total number of uniquely aligned reads and with the scale set to reads per 10^8 sequences. The outcome was converted to bigwig files through the bedGraphToBigWig tool (Kent et al. 2010) and uploaded to the UCSC genome browser (James Kent et al. 2002).

Metagene analysis

The read density metagene plots in **Figures 3E-H** and **Figure 5E,F** were created with deepTools (version 3.0.2) (Ramírez et al. 2016). Metagenes with normalized gene size (Figure 3) have bins of 10 bp while all other metagene plots in this study have single nucleotide resolution. Normalized gene and intron lengths (**Figure 3E-H**) were obtained through the scale-regions option. Exon-intron junctions without normalized lengths were obtained using the reference-option set to the 3'SS or the 5'SS. For normalization, we divided the number of reads at each nucleotide (or bin) by the total number

of reads in the entire genomic region under analysis. These values were then used to calculate the mean for each nucleotide, and the results were plotted in an arbitrary units (A.U.) ranging from 0 to 1.

The peak density metagene plots in **Figures 4** and **7** were prepared using custom Python and R scripts (https://github.com/rosinaSav/dNETseq_code). The peak density value represents the proportion of introns/exons that overlap with a peak at that position. Only internal fully coding exons that were at least 100 nucleotides long were included. In addition, the intron just upstream of the exon had to be at least 50 nt long. For **Figure 7D-F**, further filtering based on read coverage was performed (see below). Note that exons shorter than 150 nucleotides contribute both to the upstream and downstream exonic proportion of the plot.

Immediate splicing analysis

The immediate splicing analysis was performed solely on the S5P data sets. Only the 117 previously annotated pre-MBT genes (Chen et al. 2013) were analysed for early data sets. Reads were considered as spliced if they contained 'N's in the CIGAR string, in a position corresponding to an annotated intron. Reads that overlapped both the (unspliced) intron and the downstream exon were considered as unspliced. In both cases, only reads where the 3' end was located at least 5 nt downstream of the 3' ss were included, to avoid analysing misaligned reads whose 3' end should have mapped to the end of the upstream exon instead. Spliced reads that had the 5' end mapped to the upstream exon and the 3' end mapped to the intron were considered indicative of recursive splicing if the first nucleotide of the downstream end (indicative of the ratchet point position) matched the second G in the AGGT canonical splicing motif. If the last nucleotide of a read matched the last nucleotide of an exon, it was considered a splicing intermediate read and not representative of nascent RNA. A splicing ratio was calculated by dividing the number of nascent RNA spliced reads by the sum of the number of spliced and unspliced nascent RNA reads, only including reads whose 3' ends mapped to the first 100 nt of the downstream exon. Only fully coding internal exons at least 100 nt long were considered (exceptionally, in **Figure 6D, J**, **K** and **Figure S6N, O**, the 3' most coding exon was also analysed). Finally, we performed filtering to remove exons where the read coverage was too low to allow for

robust estimation of the splicing ratio. The relevant threshold was calculated for each dataset separately. We calculated the total proportion of spliced reads out of all spliced/unspliced reads for the dataset to obtain the expected splicing ratio. We then performed a binomial test to know the probability of sampling only spliced/unspliced reads by chance under the null that the true splicing ratio equalled this expectation. We set the threshold as the lowest number of reads that had to be sampled for the probability to be below 0.01. Through his procedure, the threshold was set at >=10 reads for replicate 1 and 2 of the late data set (no terminal coding exons), at >=11/10 reads for replicate 1/2 of the late data set including terminal coding exons, and at >=14/9 reads for replicate 1/2 of the early data set (terminal coding exons always included).

Gene architecture and nucleotide composition analysis

Gene architecture and nucleotide composition parameters were calculated using custom Python and R scripts based on Ensembl annotations for dm6.18 (Cunningham et al. 2019). Splice site strength scores were calculated using MaxEntScan (Yeo and Burge 2004) with default parameters. Significance testing was performed using Kruskal-Wallis tests with a Bonferroni correction for multiple comparisons, with the correction applied separately for either replicate. For predictors where the corrected *P*-value was <0.05, Dunn's test was performed on the pairwise comparisons using *R* package *dunn.test* (Dinno 2017). The sequence logo in **Figure 4D** was generated using the *seqLogo* package version 1.52.0 in R (Bembom 2019).

Data access

All raw and processed sequencing data generated in this study have been submitted to the NCBI Gene Expression Omnibus (GEO; https://www.ncbi.nlm.nih.gov/geo/) under accession number GSE152585. The Python code used is available at https://github.com/rosinaSav/dNETseq_code and https://github.com/kennyrebelo.

Acknowledgements

We thank Takayuki Nojima and Nicholas Proudfoot (University of Oxford, UK) for critical discussion. This work was supported by funding to M.C.-F. (Fundação para a Ciência e Tecnologia, FCT/ Ministério da Ciência, Tecnologia e Ensino Superior - Fundos do Orçamento de Estado (UIDB/50005/2020), and FCT/FEDER/POR Lisboa 2020, Programa Operacional Regional de Lisboa PORTUGAL 2020, grant LISBOA-01-0145-FEDER-016394) and to R.G.M (FCT grant PTDC/BIA-BID/28441/2017). P.P. was a recipient of a FCT fellowship (SFRH/BD/109689/2015). R.S. was a recipient of an EMBO Long-Term Fellowship (EMBO ALTF 101-2019).

Author Contributions

P.P. performed all molecular biology experiments. K.R. performed the majority of the bioinformatics analyses. R.S. performed additional analyses of splicing kinetics and developed the peak caller for detecting putative pause sites. P.P., R.S., R.G.M. and M.C.-F conceived the study and wrote the paper.

Disclosure

The authors declare that they have no competing interests.

SUPPLEMENTARY FIGURE LEGENDS

Figure S1. **(A)** For each *d*NET-seq library prepared, the number of total reads and of uniquely aligned reads is indicated. **(B, C)** Density of uniquely aligned reads per gene (RPKM in log2 scale) for two *d*NET-seq/S5P and *d*NET-seq/S2P biological replicates from late embryos (Pearson's correlation, R = 0.92; R = 0.96). **(D)** Histogram of the read lengths in *d*NET-seq/S5P data from late embryos. (**E**) For each *d*NET-seq library generated, the number of uniquely aligned reads corresponding to nascent transcripts is indicated. **(F)** Length of sequenced nascent RNA (in nucleotides).

Figure S2. (**A**) *d*NET-seq/S5P profile over the U6 snRNA gene in the late dataset (replicate 1). (**B**) Frequency of peaks corresponding to splicing intermediates (green) detected by *d*NET-seq/S5P on exons of genes expressed in late embryos. Genes were grouped into quartiles (Q) based on their *d*NET-seq read density.

Figure S3. **(A-D)** *d*NET-seq/S5P and RNA-seq profiles over maternal genes in early embryos: *nanos* (**A**), *gurken* (**B**), *Rab32* (**C**) and *pumilio (pum)* (**D**). **(E-F)** *d*NET-seq/S5P and RNA-seq profiles over pre-MBT genes in early embryos: *fushi tarazu* (**E**) and *odd skipped (odd)* (**F**). **(G-H)** *d*NET-seq/S5P and RNA-seq profiles over MBT genes in late embryos: *His3.3A* (**G**) and *twinstar (tsr)* (**H**). Reads that aligned to the positive strand are in blue, and reads that aligned to the negative strand are in red. The direction of transcription is indicated by an arrow.

Figure S4. **(A-C)** Identification of transcriptionally active genes based on *d*NET-seq signal along the gene body in late embryos. **(A)** Read density distribution in intergenic regions (gene deserts). The red dashed line represents the 90th percentile of read density in all intergenic regions analysed. **(B)** Read density distribution per gene (RPKM) represented in Log2 scale. The 90th percentile of read density over gene deserts is set as threshold (red dashed line). **(C)** Comparison of read density per active gene (RPKM in log2 scale) between the indicated datasets. Total number of active genes identified in each dataset is indicated (*n*). Venn diagrams show common active genes between datasets. **(D-G)** *d*NET-seq/S5P and RNA-seq profiles over the indicated pre-MBT genes. Reads that aligned to the positive strand are in blue, and reads that aligned to the negative strand are in red. The direction of transcription is indicated by an arrow.

Figure S5. **(A)** Venn diagram comparing RPs identified in two *d*NET-seq/S2P biological replicates and in previously reported studies (Joseph et al. 2018; Duff et al. 2015).

Figure S6. In all panels, unless otherwise specified, only introns from transcriptionally active genes where the downstream exon is a fully coding internal exon at least 100 nt long were included. In

addition, enough spliced/unspliced reads had to end within the first 100 exonic nucleotides that obtaining a splicing ratio (SR) of 0 or 1 by chance alone was highly unlikely (see the methods section for details). For genes expressed in late embryos, this threshold was 10 reads for both replicates. For pre-MBT genes, it was 14 for replicate 1 and 9 for replicate 2. (**A**) Values of *d*NET-seq SRs estimated in two biological replicates of *d*NET-seq/S5P datasets for pre-MBT genes in the early data sets (Spearman correlation, $\rho = \sim 0.775$, $P \sim 1.348 * 10^{-14}$). (**B-O**) show *d*NET-seq/S5P data for the late datasets. **(B)** Histogram of SRs for *d*NET-seq/S5P (replicate 2). N = 4510, with 796 introns with SR = 0 and 254 introns with SR = 1. **(C-O)** show SR plotted out against several gene architecture parameters (**(C-E)** for replicate 1 and **(F-O)** for replicate 2). For sample sizes and statistical tests, see **Supplementary Table 1**. In **(C-I, M-O)**, the bin ranges have been set so that intron numbers would be as equal possible between bins. ss: splice site.

REFERENCES

Alexander RD, Innocente SA, Barrass JD, Beggs JD. 2010. Splicing-dependent RNA polymerase pausing in yeast. *Mol Cell* **40**: 582–593.

Ali-Murthy Z, Lott SE, Eisen MB, Kornberg TB. 2013. An Essential Role for Zygotic Expression in the Pre-Cellular Drosophila Embryo. *PLoS Genet* **9**.

Alpert T, Herzel L, Neugebauer KM. 2017. Perfect timing: splicing and transcription rates in living cells. *WIREs RNA* **8**.

Ameur A, Zaghlool A, Halvardson J, Wetterbom A, Gyllensten U, Cavelier L, Feuk L. 2011. Total RNA sequencing reveals nascent transcription and widespread co-transcriptional splicing in the human brain. *Nat Struct Mol Biol* **18**: 1435–1440.

Artieri CG, Fraser HB. 2014. Transcript length mediates developmental timing of gene expression across drosophila. *Mol Biol Evol* **31**: 2879–2889.

Aslanzadeh V, Huang Y, Sanguinetti G, Beggs JD. 2018. Transcription rate strongly affects splicing fidelity and cotranscriptionality in budding yeast. *Genome Res* **28**: 203–213.

Bembom O. 2019. seqLogo: Sequence logos for DNA sequence alignments. R package version 1.52.0.

Berget SM. 1995. Exon Recognition in Vertebrate Splicing. *J Biol Chem* **270**: 2411–2414.

Beyer AL, Osheim YN. 1988. Splice site selection, rate of splicing, and alternative splicing on nascent transcripts. *Genes Dev* **2**: 754–765.

Blythe SA, Wieschaus EF. 2015a. *Coordinating Cell Cycle Remodeling with Transcriptional Activation at the Drosophila MBT*. 1st ed. Elsevier Inc.

Blythe SA, Wieschaus EF. 2015b. Zygotic Genome Activation Triggers the DNA Replication Checkpoint at the Midblastula Transition Article Zygotic Genome Activation Triggers the DNA Replication Checkpoint at the Midblastula Transition. *Cell* **160**: 1–13.

Brugiolo M, Herzel L, Neugebauer KM. 2013. Counting on co-transcriptional splicing. *F1000Prime Rep* **5**.

Burnette JM, Miyamoto-Sato E, Schaub MA, Conklin J, Lopez AJ. 2005. Subdivision of large introns

in Drosophila by recursive splicing at nonexonic elements. *Genetics* **170**: 661–674.

Bushnell B, Rood J, Singer E. 2017. BBMerge – Accurate paired shotgun read merging via overlap. *PLoS One* **12**.

Campos-Ortega JA. 1985. Genetics of early neurogenesis in Drosophila melanogaster. *Trends Neurosci* **8**: 245–250.

Carrillo Oesterreich F, Herzel L, Straube K, Hujer K, Howard J, Neugebauer KM. 2016. Splicing of Nascent RNA Coincides with Intron Exit from RNA Polymerase II. *Cell* **165**: 372–381.

Carrillo Oesterreich F, Preibisch S, Neugebauer KM. 2010. Global analysis of nascent RNA reveals transcriptional pausing in terminal exons. *Mol Cell* **40**: 571–581. http://dx.doi.org/10.1016/j.molcel.2010.11.004.

Chen K, Johnston J, Shao W, Meier S, Staber C, Zeitlinger J. 2013. A global change in RNA polymerase II pausing during the Drosophila midblastula transition. *Elife* **2013**.

Churchman LS, Weissman JS. 2011. Nascent transcript sequencing visualizes transcription at nucleotide resolution. *Nature* **469**: 368–373.

Core LJ, Waterfall JJ, Lis JT. 2008. Nascent RNA Sequencing Reveals Widespread Pausing and Divergent Initiation. *Science* **322**: 1845–1849.

Cunningham F, Achuthan P, Akanni W, Allen J, Amode MR, Armean IM, Bennett R, Bhai J, Billis K, Boddu S, et al. 2019. Ensembl 2019. *Nucleic Acids Res* **47**: D745–D751.

Dahlberg O, Shilkova O, Tang M, Holmqvist PH, Mannervik M. 2015. P-TEFb, the Super Elongation Complex and Mediator Regulate a Subset of Non-paused Genes during Early Drosophila Embryo Development. *PLoS Genet* **11**.

David CJ, Boyne AR, Millhouse SR, Manley JL. 2011. The RNA polymerase II C-terminal domain promotes splicing activation through recruitment of a U2AF65-Prp19 complex. *Genes Dev* **25**: 972–982.

de Almeida SF, Carmo-Fonseca M. 2008. The CTD role in cotranscriptional RNA processing and surveillance. *FEBS Lett* **582**: 1971–1976.

De Conti L, Baralle M, Buratti E. 2013. Exon and intron definition in pre-mRNA splicing. *Wiley Interdiscip Rev RNA* **4**: 49–60.

De Renzis S, Elemento O, Tavazoie S, Wieschaus EF. 2007. Unmasking activation of the zygotic genome using chromosomal deletions in the Drosophila embryo. *PLoS Biol* **5**: 1036–1051.

Dingwall C, Lomonossoff GP, Laskey RA. 1981. High sequence specificity of micrococcal nuclease. *Nucleic Acids Res* **9**: 2659–2674.

Dinno A. 2017. dunn.test: Dunn's Test of Multiple Comparisons Using Rank Sums. R package version 1.3.5. https://cran.r-project.org/package=dunn.test.

Dobin A, Davis CA, Schlesinger F, Drenkow J, Zaleski C, Jha S, Batut P, Chaisson M, Gingeras TR. 2013. STAR: Ultrafast universal RNA-seq aligner. *Bioinformatics* **29**: 15–21.

Drexler HL, Choquet K, Churchman LS. 2020. Splicing Kinetics and Coordination Revealed by Direct Nascent RNA Sequencing through Nanopores. *Mol Cell* **77**: 985-998.e8.

Duff MO, Olson S, Wei X, Garrett SC, Osman A, Bolisetty M, Plocik A, Celniker SE, Graveley BR. 2015. Genome-wide identification of zero nucleotide recursive splicing in Drosophila. *Nature* **521**: 376–379.

Emili A, Shales M, McCracken S, Xie W, Tucker PW, Kobayashi R, Blencowe BJ, Ingles CJ. 2002. Splicing and transcription-associated proteins PSF and p54nrb/NonO bind to the RNA polymerase II CTD. *Rna* **8**: 1102–1111.

Erickson JW, Cline TW. 1993. A bZIP protein, sisterless-a, collaborates with bHLH transcription factors early in Drosophila development to determine sex. *Genes Dev* **7**: 1688–1702.

Fong N, Kim H, Zhou Y, Ji X, Qiu J, Saldi T, Diener K, Jones K, Fu XD, Bentley DL. 2014. Pre-mRNA splicing is facilitated by an optimal RNA polymerase II elongation rate. *Genes Dev* **28**: 2663–2676.

Fox-Walsh KL, Dou Y, Lam BJ, Hung S -p., Baldi PF, Hertel KJ. 2005. The architecture of pre-mRNAs affects mechanisms of splice-site pairing. *Proc Natl Acad Sci* **102**: 16176–16181.

Fukaya T, Lim B, Levine M. 2017. Rapid Rates of Pol II Elongation in the Drosophila Embryo. *Curr Biol* **27**: 1387–1391.

Gaffney DJ, McVicker G, Pai AA, Fondufe-Mittendorf YN, Lewellen N, Michelini K, Widom J, Gilad Y, Pritchard JK. 2012. Controls of Nucleosome Positioning in the Human Genome. *PLoS Genet* **8**.

Gelfman S, Cohen N, Yearim A, Ast G. 2013. DNA-methylation effect on cotranscriptional splicing is dependent on GC architecture of the exon-intron structure. *Genome Res* **23**: 789–799.

Görnemann J, Barrandon C, Hujer K, Rutz B, Rigaut G, Kotovic KM, Faux C, Neugebauer KM, Séraphin B. 2011. Cotranscriptional spliceosome assembly and splicing are independent of the Prp40p WW domain. *Rna* **17**: 2119–2129.

Graveley BR, Brooks AN, Carlson JW, Duff MO, Landolin JM, Yang L, Artieri CG, Baren MJ Van, Boley N, Booth BW, et al. 2011. The Developmental Transcriptome of Drosophila melanogaster. *Nature* **471**: 473–479.

Guilgur LG, Prudêncio P, Sobral D, Liszekova D, Rosa A, Martinho RG. 2014. Requirement for highly efficient pre-mRNA splicing during Drosophila early embryonic development. *Elife* **3**.

Harlen KM, Trotta KL, Smith EE, Mosaheb MM, Fuchs SM, Churchman LS. 2016. Comprehensive RNA Polymerase II Interactomes Reveal Distinct and Varied Roles for Each Phospho-CTD Residue. *Cell Rep* **15**: 2147–2158.

Hatton AR, Subramaniam V, Lopez AJ. 1998. Generation of alternative Ultrabithorax isoforms and stepwise removal of a large intron by resplicing at exon-exon junctions. *Mol Cell* **2**: 787–796.

Herzel L, Straube K, Neugebauer KM. 2018. Long-read sequencing of nascent RNA reveals coupling among RNA processing events. 1008–1019.

Heyn P, Kircher M, Dahl A, Kelso J, Tomancak P, Kalinka AT, Neugebauer KM. 2014. The earliest transcribed zygotic genes are short, newly evolved, and different across species. *Cell Rep* **6**: 285–292.

Hörz W, Altenburger W. 1981. Sequence specific cleavage of DNA by micrococcal nuclease. *Nucleic Acids Res* **9**: 2643–2658.

Hoskins RA, Landolin JM, Brown JB, Sandler JE, Takahashi H, Lassmann T, Booth BW, Zhang D, Wan KH, Yang L, et al. 2011. Genome-wide analysis of promoter architecture in Drosophila melanogaster. *Genome Res* **21**: 182–192.

Hsin JP, Manley JL. 2012. The RNA polymerase II CTD coordinates transcription and RNA processing. *Genes Dev* **26**: 2119–2137.

James Kent W, Sugnet CW, Furey TS, Roskin KM, Pringle TH, Zahler AM, Haussler D. 2002. The

human genome browser at UCSC. *Genome Res* **12**: 996–1006.

Ji J-Y, Squirrell JM, Schubiger G. 2004. Both Cyclin B levels and DNA-replication checkpoint control the early embryonic mitoses in Drosophila Jun-Yuan. *Development* **131**: 401–411.

Jonkers I, Kwak H, Lis JT. 2014. Genome-wide dynamics of Pol II elongation and its interplay with promoter proximal pausing, chromatin, and exons. *Elife* **2014**.

Joseph B, Kondo S, Lai EC. 2018. Short cryptic exons mediate recursive splicing in Drosophila. *Nat Struct Mol Biol* **25**: 365–371.

Kent WJ, Zweig AS, Barber G, Hinrichs AS, Karolchik D. 2010. BigWig and BigBed: Enabling browsing of large distributed datasets. *Bioinformatics* **26**: 2204–2207.

Keren H, Lev-Maor G, Ast G. 2010. Alternative splicing and evolution: Diversification, exon definition and function. *Nat Rev Genet* **11**: 345–355. http://dx.doi.org/10.1038/nrg2776.

Khodor YL, Menet JS, Tolan M, Rosbash M. 2012. Cotranscriptional splicing efficiency differs dramatically between Drosophila and mouse. *RNA* **18**: 2174–2186.

Khodor YL, Rodriguez J, Abruzzi KC, Tang CHA, Marr MT, Rosbash M. 2011. Nascent-seq indicates widespread cotranscriptional pre-mRNA splicing in Drosophila. *Genes Dev* **25**: 2502–2512.

Kimura H, Tao Y, Roeder RG, Cook PR. 1999. Quantitation of RNA Polymerase II and Its Transcription Factors in an HeLa Cell: Little Soluble Holoenzyme but Significant Amounts of Polymerases Attached to the Nuclear Substructure. *Mol Cell Biol* **19**: 5383–5392.

Kwak H, Fuda NJ, Core LJ, Lis JT. 2013. Precise maps of RNA polymerase reveal how promoters direct initiation and pausing. *Science* **339**: 950–953.

Kwasnieski JC, Orr-Weaver TL, Bartel DP. 2019. Early genome activation in Drosophila is extensive with an initial tendency for aborted transcripts and retained introns. *Genome Res* **29**: 1188–1197.

Larson MH, Mooney RA, Peters JM, Windgassen T, Nayak D, Gross CA, Block SM, Greenleaf WJ, Landick R, Weissman JS. 2014. A pause sequence enriched at translation start sites drives transcription dynamics in vivo. *Science* **344**: 1042–1047.

Laver JD, Marsolais AJ, Smibert CA, Lipshitz HD. 2015. *Regulation and Function of Maternal Gene Products During the Maternal-to-Zygotic Transition in Drosophila*. 1st ed. Elsevier Inc.

http://dx.doi.org/10.1016/bs.ctdb.2015.06.007.

Li H, Handsaker B, Wysoker A, Fennell T, Ruan J, Homer N, Marth G, Abecasis G, Durbin R. 2009. The Sequence Alignment/Map format and SAMtools. *Bioinformatics* **25**: 2078–2079.

Lott SE, Villalta JE, Schroth GP, Luo S, Tonkin LA, Eisen MB. 2011. Noncanonical compensation of zygotic X transcription in early Drosophila melanogaster development revealed through single-embryo RNA-Seq. *PLoS Biol* **9**.

Lund E, Dahlberg JE. 1992. Cyclic 2 ', 3 "-Phosphates and Nontemplated Nucleotides at the 3" End of Spliceosomal U6 Small Nuclear RNAs. *Science* **255**: 327–330.

Martin M. 2011. Cutadapt removes adapter sequences from high-throughput sequencing reads. *EMBnet.journal* **17**: 10–12.

Martin RM, Rino J, Carvalho C, Kirchhausen T, Carmo-Fonseca M. 2013. Live-Cell Visualization of Pre-mRNA Splicing with Single-Molecule Sensitivity. *Cell Rep* **4**: 1144–1155.

Martinho RG, Guilgur LG, Prudêncio P. 2015. How gene expression in fast-proliferating cells keeps pace. *BioEssays* **37**: 514–524.

Maslon MM, Braunschweig U, Aitken S, Mann AR, Kilanowski F, Hunter CJ, Blencowe BJ, Kornblihtt AR, Adams IR, Cáceres JF. 2019. A slow transcription rate causes embryonic lethality and perturbs kinetic coupling of neuronal genes. *EMBO J* **38**.

Mayer A, Di Iulio J, Maleri S, Eser U, Vierstra J, Reynolds A, Sandstrom R, Stamatoyannopoulos JA, Churchman LS. 2015. Native elongating transcript sequencing reveals human transcriptional activity at nucleotide resolution. *Cell* **161**: 541–554.

Morris DP, Greenleaf AL. 2000. The splicing factor, Prp40, binds the phosphorylated carboxyl-terminal domain of RNA Polymerase II. *J Biol Chem* **275**: 39935–39943.

Nojima T, Gomes T, Carmo-Fonseca M, Proudfoot NJ. 2016. Mammalian NET-seq analysis defines nascent RNA profiles and associated RNA processing genome-wide. *Nat Protoc* **11**: 413–428.

Nojima T, Gomes T, Grosso ARF, Kimura H, Dye MJ, Dhir S, Carmo-Fonseca M, Proudfoot NJ. 2015. Mammalian NET-seq reveals genome-wide nascent transcription coupled to RNA processing. *Cell* **161**: 526–540.

Nojima T, Rebelo K, Gomes T, Grosso AR, Proudfoot NJ, Carmo-Fonseca M. 2018. RNA

Polymerase II Phosphorylated on CTD Serine 5 Interacts with the Spliceosome during Co-transcriptional Splicing. *Mol Cell* **72**: 369-379.e4.

Pai AA, Henriques T, McCue K, Burkholder A, Adelman K, Burge CB. 2017. The kinetics of pre-mRNA splicing in the Drosophila genome and the influence of gene architecture. *Elife* **6**.

Pai AA, Paggi JM, Yan P, Adelman K, Burge CB. 2018. Numerous recursive sites contribute to accuracy of splicing in long introns in flies. *PLoS Genet* **14**.

Pertea M, Pertea GM, Antonescu CM, Chang TC, Mendell JT, Salzberg SL. 2015. StringTie enables improved reconstruction of a transcriptome from RNA-seq reads. *Nat Biotechnol* **33**: 290–295.

Pritchard DK, Schubiger G. 1996. Activation of transcription in Drosophila embryos is a gradual process mediated by the nucleocytoplasmic ratio. *Genes Dev* **10**: 1131–1142.

Prudêncio P, Rebelo K, Grosso AR, Martinho RG, Carmo-fonseca M. 2020. Analysis of Mammalian Native Elongating Transcript sequencing (mNET-seq) high-throughput data. *Methods* **178**: 89–95.

Quinlan AR, Hall IM. 2010. BEDTools: A flexible suite of utilities for comparing genomic features. *Bioinformatics* **26**: 841–842.

Ramírez F, Ryan DP, Grüning B, Bhardwaj V, Kilpert F, Richter AS, Heyne S, Dündar F, Manke T. 2016. deepTools2: a next generation web server for deep-sequencing data analysis. *Nucleic Acids Res* **44**: W160–W165.

Reimer KA, Mimoso C, Adelman K, Neugebauer KM. 2020. Rapid and Efficient Co-Transcriptional Splicing Enhances Mammalian Gene Expression. *bioRxiv*.

Robberson BL, Cote GJ, Berget SM. 1990. Exon Definition May Facilitate Splice Site Selection in RNAs with Multiple Exons. *Mol Cell Biol* **10**: 84–94.

Rothe M, Pehl M, Taubert H, Jäckle H. 1992. Loss of gene function through rapid mitotic cycles in the Drosophila embryp. *Nature* **359**: 156–159.

Sandler JE, Irizarry J, Stepanik V, Dunipace L, Amrhein H, Stathopoulos A. 2018. A Developmental Program Truncates Long Transcripts to Temporally Regulate Cell Signaling. *Dev Cell* **47**: 773-784.e6.

Saunders A, Core LJ, Sutcliffe C, Lis JT, Ashe HL. 2013. Extensive polymerase pausing during

Drosophila axis patterning enables high-level and pliable transcription. *Genes Dev* **27**: 1146–1158.

Schlackow M, Nojima T, Gomes T, Dhir A, Carmo-Fonseca M, Proudfoot NJ. 2017. Distinctive Patterns of Transcription and RNA Processing for Human lincRNAs. *Mol Cell* **65**: 25–38.

Shermoen AW, O'Farrell PH. 1991. Progression of the Cell Cycle through Mitosis Leads to Abortion of Nascent Transcripts. *Cell* **67**: 303–310.

Sterner DA, Carlo T, Berget SM. 1996. Architectural limits on split genes. *Proc Natl Acad Sci USA* **93**: 15081–15085.

Tadros W, Lipshitz HD. 2009. The maternal-to-zygotic transition: A play in two acts. *Development* **136**: 3033–3042.

Veloso A, Kirkconnell KS, Magnuson B, Biewen B, Paulsen MT, Wilson TE, Ljungman M. 2014. Rate of elongation by RNA polymerase II is associated with specific gene features and epigenetic modifications. *Genome Res* **24**: 896–905.

Windhager L, Bonfert T, Burger K, Ruzsics Z, Krebs S, Kaufmann S, Malterer G, L'Hernault A, Schilhabel M, Schreiber S, et al. 2012. Ultrashort and progressive 4sU-tagging reveals key characteristics of RNA processing at nucleotide resolution. *Genome Res* **22**: 2031–2042.

Yeo G, Burge CB. 2004. Maximum entropy modeling of short sequence motifs with applications to RNA splicing signals. *J Comput Biol* **11**: 377–394.

Yuan K, Seller CA, Shermoen AW, Farrell PHO. 2016. Timing the Drosophila Mid-Blastula Transition: A Cell Cycle-Centered View. *Trends Genet* **32**: 496–507. http://dx.doi.org/10.1016/j.tig.2016.05.006.

Zhu L, Zhang Y, Zhang W, Yang S, Chen J, Tian D. 2009. Patterns of exon-intron architecture variation of genes in eukaryotic genomes. *BMC Genomics* **10**.